

3D fluid flow in fault zones of crystalline basement rocks (Poehla-Tellerhaeuser Ore Field, Ore Mountains, Germany)

P. ACHTZIGER-ZUPANČIČ¹, S. LOEW¹, A. HILLER² AND G. MARIETHOZ^{1,3}

¹ETH Zürich, Geologic Institute, Chair of Engineering Geology, Zürich, Switzerland; ²Division Engineering/Radiation Protection, Wismut GmbH, Chemnitz, Germany; ³Institute of Earth Surface Dynamics (IDYST), University of Lausanne, Lausanne, Switzerland

ABSTRACT

A comprehensive dataset for discrete groundwater inflows to mines in the Poehla-Tellerhaeuser Ore Field and the mining scale fault zones has been compiled from unpublished data recorded by eastern German and Soviet hydrogeologists at the Soviet-German stock company (SDAG) Wismut. This dataset has been analyzed to provide novel insights into the 3D distribution of preferential groundwater pathways and the impacts of faulting on the distribution of hydraulic parameters in crystalline rocks at site scale. The sampled 1030 discrete inflows include flow rates ranging from 1.7E-8 to 3.7E-2 m³ sec⁻¹, which were transformed into mesoscale fracture transmissivity values ranging between 3E-13 and 2E-4 m² sec⁻¹. These mesoscale fracture transmissivities were spatially correlated with fault zones exhibiting trace lengths between 0.3 and 30 km, which were mainly formed during and reactivated several times since Variscan orogeny. The statistical correlations are based on a 3D geological model composed of 14 litho-stratigraphic units and 131 mining scale faults, separated into five main strike directions. These fault zones strongly overlap and cover about 90% of the investigated rock mass volume with a decreasing percentage of overlap in the investigated depth range (0–900 mbgs). 97% of all inflows are located within fault damage zones, and most of the flow occurs within the overlap of multiple fault damage zones. A dimensionless hydraulic model for the distribution of flow Q as a function of the position x within mining scale fault zones has been derived as $Q = 1.1e^{-4.5x}$ (where x decreases from the fault core to the protolith and the exponent varies as a function of fault orientation). 75–95% of the flow occurs within the inner 50% of the damage zone, and mainly NW-SE and NE-SW striking mining scale faults are transmissive. The orientations of conductive mesoscale fractures within these damage zones show a larger variability than the corresponding mining scale faults.

Key words: 3D geologic modelling, crystalline basement, fault zone, fault zone architecture, fault zone hydrogeology, fluid flow, hydraulic model, mine water drainage, tectonics

Received 19 January 2016; accepted 3 August 2016

Corresponding author: P. Achtziger-Zupančič, ETH Zürich, Geologic Institute, Chair of Engineering Geology, Sonneggstr. 5, CH-8092 Zürich, Switzerland.

Email: peter.achtziger@erdw.ethz.ch. Tel: +41 44 632 23 62. Fax: +41 44 633 11 08.

Geofluids (2016)

INTRODUCTION

Understanding and predicting the hydraulic properties of fractured crystalline rocks at site scale has high practical relevance and economic importance within the context of, for example, the production of hydrothermal and petrothermal energy, groundwater resources, earthquake prediction, geological waste disposal, mining, orebody formation, and underground constructions. But, although groundwater flow at site scales has been studied for decades (e.g., Massonnat 1981; Maréchal 1998; Masset & Loew 2010; Seebach *et al.* 2014), our capability to reliably predict flow

conditions in fractured rocks is still very limited (Berkowitz 2002; Ingebretsen & Manning 2010). Flow rates depend on a number of intrinsic factors, such as transmissivity/permeability, storativity/specific storage, pressure head, and fluid viscosity (e.g., Snow 1965; Bear *et al.* 1993). Tectonic structures and their architecture are most important extrinsic factors for water flow on any scale in low porosity rocks such as crystalline basement as they provide porosity and connectivity (e.g., Long *et al.* 1996). Other examples for extrinsic factors influencing fluid flow in fractured rock are the coupled thermo-hydro-mechanical-chemical (THMC) properties of the host rock, the existence of

fracture infill and its appearance, and *in situ* stress conditions (e.g., Rutqvist & Stephansson 2003; Micklethwaite *et al.* 2010; Bense *et al.* 2013; Stober & Bucher 2015; Ingebritsen & Gleeson 2015). The focus of this article is on the 3D relationships between faulting and fracture transmissivity at the scale ranging from a mining drift to an entire ore field in crystalline rocks, based on a unique 3D dataset from the Ore Mountains in Saxony.

Fault zone architecture

Different authors described fault zones to consist of a fault core surrounded by a damage zone and the protolith itself (e.g., Sibson 1982; Chester & Logan 1987; Forster & Evans 1991; Byerlee 1993). Although this is the standard architecture of faults, at different sites the fault core was missing (especially in immature faults). Therefore, Caine *et al.* (1996) described a conceptual model for fault zone related fluid flow, which is based on the relative extent of fault core and fault damage zones by comparing fault zone architectures and their permeability structure in different settings.

The damage zones typically act as ‘conduits’ with permeabilities usually several orders of magnitude higher than those measured in the fault core (Caine *et al.* 1996; Evans *et al.* 1997; Seront *et al.* 1998; Caine & Forster 1999; Sutherland *et al.* 2012; Welch & Allen 2014). Water flow within the damage zone is mainly dependent on the orientation of the fault within the current stress field, the fracture connectivity, the aperture distribution, and fracture roughness (Gale 1982; Caine *et al.* 1996, 2010; Evans *et al.* 1997; Ball *et al.* 2010; Faulkner *et al.* 2010; Welch & Allen 2014). Fracture density and permeability are expected to decrease with increasing distance to the fault core, measured perpendicularly to the fault strike (Beaudoin *et al.* 2006; Faulkner *et al.* 2006, 2010; Caine *et al.* 2010; Bense *et al.* 2013). Fault systems composed of overlapping fault zones and multiple repetitions of fault core and damage zones are even more complex (Wallace & Morris 1986; Sibson 1996; Miller & Nur 2000; Faulkner *et al.* 2003, 2010; Benedek & Molnár 2013; Bense *et al.* 2013).

Fault zone orientation, stress, and permeability

Statistical investigations of fracture and fault orientation, regional stress fields and Mohr-Coulomb frictional strength show at many sites that critically stressed fractures and faults correlate with increased fracture transmissivity (e.g., Barton *et al.* 1995; Talbot & Sirat 2001; Ingebritsen & Appold 2012). Additionally, some authors state that secondary faults not oriented favorably within the regional stress field may be permeable due to stress rotation around a governing fault which slips regularly (see Faulkner *et al.*

2010; Micklethwaite *et al.* 2010; Bense *et al.* 2013; Tsang & Niemi 2013 and references therein). Topographic effects and alteration cause stress perturbation close to the surface which intensifies dispersion of transmissive fracture orientation (Lawson 1968; Gale 1982; Pan *et al.* 1994, 1995; Henriksen 1995; Lachassagne *et al.* 2011).

Study objectives and approach

As shown above, substantial work on fault zone hydrology has been conducted already, but is mostly related to single faults (e.g., Caine *et al.* 1996; Aydin 2000; Berkowitz 2002; Mori *et al.* 2003; Faulkner *et al.* 2010; Bense *et al.* 2013; Gentier *et al.* 2013) and only rarely to fault networks on the decameter to kilometer scale (e.g., Bear *et al.* 1993; Rutqvist & Stephansson 2003; Neuman 2005; Micklethwaite *et al.* 2010). Past research on fault zone hydrology was related to outcrops or linear galleries, thus to 1D or 2D objects. In this study, we had the unique opportunity to study fault hydrogeology in crystalline basement rocks on a km scale in 3D. The objectives of this article are to explore and describe the 3D transmissivity pattern and the detailed interrelationships between tectonic faults and fluid flow in crystalline basement rocks at site scale. This analysis will be based on the spatial distribution, transmissivity, and orientation of conductive mesoscale fractures within and around up to kilometer scale faults in crystalline basement rocks. We relate these hydraulic properties to fault zone architecture, tectonic history, and the present day regional stress field. These dependencies are studied based on a unique 3D dataset compiled from unpublished reports for the deposits Globenstein, Haemmerlein, and Tellerhaeuser at Poehla-Tellerhaeuser Ore Field (Ore Mountains, Germany) stored at the archive of Wismut GmbH. About 1.100 discrete inflows were localized and characterized while the mine was prospected between 1968 and 1991. The statistical processing of mine inflows and geologic structures is based on a 3D geological model created with SKUA-GOCAD, ArcGIS, and Matlab scripts.

This article focusses on the impacts of fault zone orientation, fault zone structure, and structure of the fault network on 3D fluid flow in crystalline rocks at the scale of an ore field. In a companion paper, we investigate the interrelationships between hydraulic properties, lithology, depth, and metamorphic overprint in mines and galleries of the Ore Mountains in Saxony.

SITE DESCRIPTION

Ore field description

In this study, we use two different reference systems for elevation description. The nearly horizontal mine levels are

expressed in m above sea level (masl). As the topography above the excavations increases from the N (500 masl) to the S (900 masl) and hydraulic head is important for the calculation of transmissivity; inflow points are expressed in m below ground surface (mbgs).

The Poehla-Tellerhaeuser Ore Field is situated in SW Saxony, in the upper Western Ore Mountains. The mining territory lies close to the border of the Czech Republic, in the area between the towns of Schwarzenberg and Oberwiesenthal. The ore field can be subdivided (from NW to SE) into the Poehla-Globenstein Sn-W deposit, the Haemmerlein Sn deposit, and the Tellerhaeuser Sn-U deposit (Fig. 1).

Prospection at the deposit Globenstein started on the mining levels 410 and 350 masl for uranium at the end of the 1950s. The mine lacked of resources and was abandoned in 1960. Between 1961 and 1967, magnetite skarn was excavated. During the main exploration period, the deposit was investigated for tin on three levels (410, 350, and 315 masl) and with about 50 km of drillings from the surface lasting from 1974 to 1976 and from 1982 to 1988. The data compiled for the Globenstein deposit are from these latest periods.

The deposits Haemmerlein and Tellerhaeuser were under exploration for uranium in the late 1970s. The Haemmerlein–Tellerhaeuser mining section was prospected

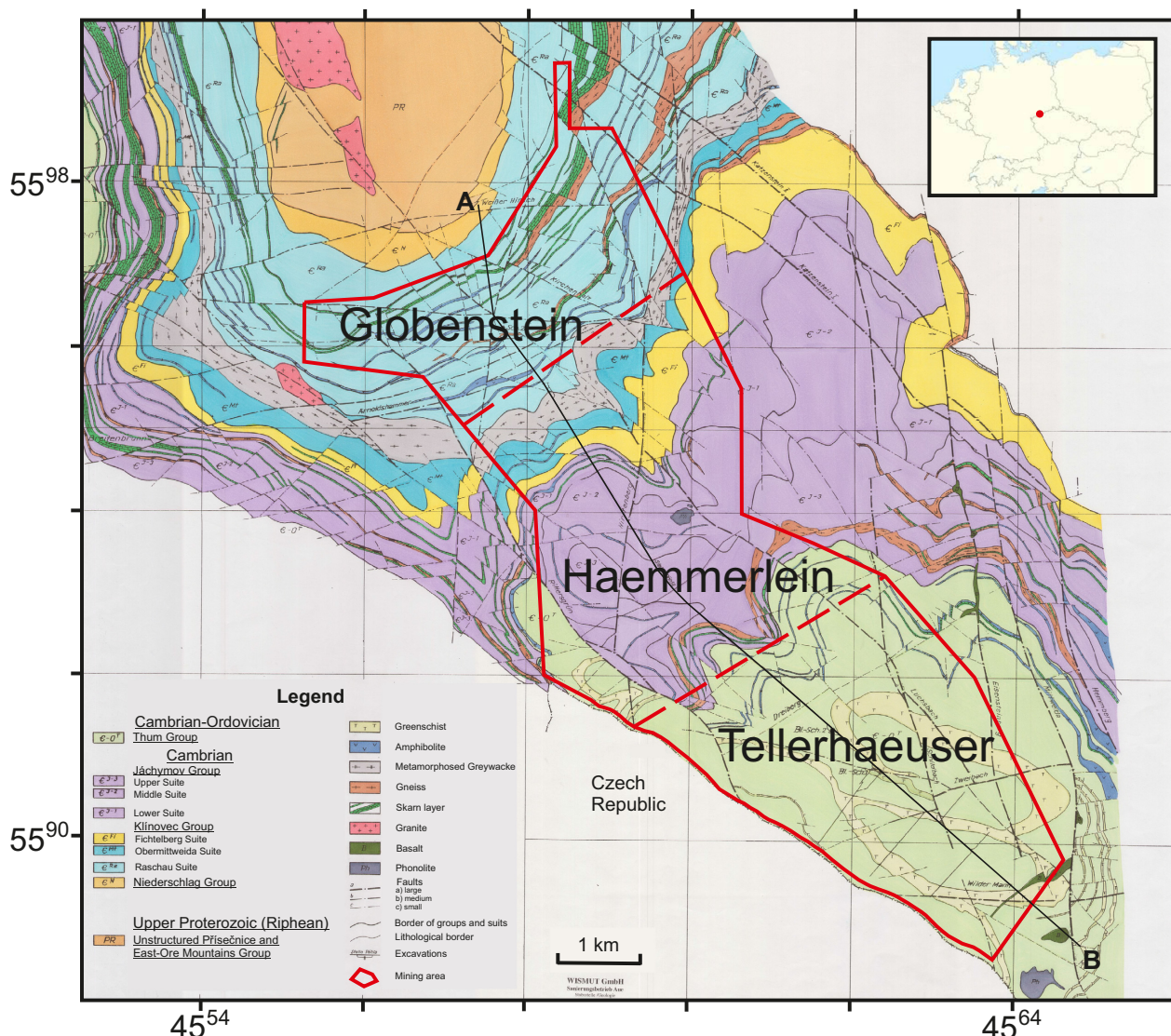


Fig. 1. The Poehla-Tellerhaeuser Ore Field area is situated within the Ore Mountains at the border between Germany and Czech Republic. From NW to SE, it is divided into the deposits Globenstein, Haemmerlein, and Tellerhaeuser. The borders of the deposits are shown schematically as the excavations follow the ore bodies along their dip to SE and might overlap in plain view. Basement rock mass consists of a prograde metamorphic series from lower greenschist to higher amphibolite facies (modified from Hiller et al. 2013).

by both surface drilling and by excavations (starting with a 7.8 km long adit). Excavations at Haemmerlein were situated at the levels 610, 590 (adit), 530, and 500 masl. The Tellerhaeuser deposit was developed by two blind shafts with main galleries at 600 m (adit), 300, 240, 180, 120, and 85 masl. Additionally, data were sampled from short galleries hosting air supply boreholes at 785 masl. After 1990, the Poehla-Tellerhaeuser Ore Field was definitively abandoned, sealed, and drowned.

The mine development was strongly driven by the orientation of the main fault clusters (Table S1). Therefore, the main prospecting grid consists of drifts striking NNW-SSE (Globenstein) to NW-SE (Haemmerlein and Tellerhaeuser) and NE-SW (all). Drifts prospecting single ore bodies followed the veins and faults hosting the ore and hence are oriented accordingly.

Geological and tectono-metamorphic setting

The Ore Mountains are an exhumed Variscan orogen consisting of a prograde series of metamorphic rocks ranging from greenschist to eclogites facies (e.g., Pälchen & Walter 2011; Sebastian 2012). Tectonically, most intensive phases occurred during Variscan orogeny (Carboniferous to Ordovician) and during the opening of the Ohře- (Eger-) Rift from Eocene to lower Miocene (Kuschka 2002). Karstification of marble/skarn lenses started 42 Ma ago and was intensified by the tilt and exhumation of the Ore Mountains as a rift shoulder of the Ohře-Rift in the period between 30 and 15 Ma (e.g., Pälchen & Walter 2011; Sebastian 2012; K.P. Stanek, unpublished report). Stress field inferred from *in situ* stress measurements and earthquake focal mechanisms suggest that the major (σ_1) and the minor (σ_3) stress component are oriented subhorizontally in NNW-SSE and ENE-WSW direction, respectively, and the intermediate stress component (σ_2) is oriented subvertically for most parts of the Ore Mountains (Grünthal *et al.* 1990; Grünthal & Stromeyer 1992; Bankwitz *et al.* 1993, 1995; Horálek *et al.* 2000; Heidbach *et al.* 2008; Buchholz *et al.* 2011; Andreani *et al.* 2014). According to Berger *et al.* 2011, the only reasonable measurements of the stress magnitudes in this area were conducted about 30 km NW from Poehla-Tellerhaeuser Ore

Field in about 2000 m depth resulting in $\sigma_1 = 80\text{--}140$ MPa, $\sigma_2 = 45\text{--}60$ MPa, and $\sigma_3 = 35\text{--}45$ MPa.

The Poehla-Tellerhaeuser Ore Field is a part of the Fichtelgebirge–Erzgebirge anticline, located in the transition area between the Schwarzenberg gneiss dome structure in the north and the Tellerhaeuser–Hundsmarter syncline in the south (Figs 1 and 2). The deposits are bound to the intersection of the inter-regional NW-SE-trending Gera-Jáchymov Lineament (300 km length) and the regional ENE-WSW-striking South Erzgebirge Deep Fault Zone (40 km length).

Wall rocks comprise of Cambrian to Ordovician metasediments including several litho-stratigraphic units folded into a shallow syncline (Fig. 1–3), which is cut off at depths of 200–1000 mbgs by NW-SE-elongated dome-shaped Variscan biotite and two-mica granites (Eibenstock type). As the mines were excavated at the NW flank, the host rocks strike NE-SW and dip 8–15° SE throughout the excavations (Fig. 2). Late Hercynian aplite, lamprophyre/kersantite, granite porphyry, and occasional Tertiary phonolite dikes cut the metamorphous rocks. Subconcordant structures of blastomylonite or blastocataclasite are prevalent and mostly trend aside marble/skarn layers.

Structural geology and faulting

Detailed research about the hydromechanical behavior of faults in crystalline rock usually was conducted on scales from μm to some 100th of meters of trace length and a fault zone thickness in the range of mm to 10th of meters. The scale of faults at Poehla-Tellerhaeuser Ore Field—we call mining scale—covers a range of 0.3–30 km of trace length and 5 cm to 1.5 km of fault zone thickness (Figs 4 and 5). The structural inventory was separated into six groups based on their orientation and their formation (Table 1). Main formation time of the faults was during Variscan orogeny. Most of the faults experienced intensive multiple reactivation of which the (possibly) last ones are shown in Table 1. Additionally, the range of cumulative displacements and resulting fault damage and fault core thicknesses are shown for the fault groups.

Detailed structural descriptions of faults, veins, and shear lenses are available from about 60 outcrops (of several

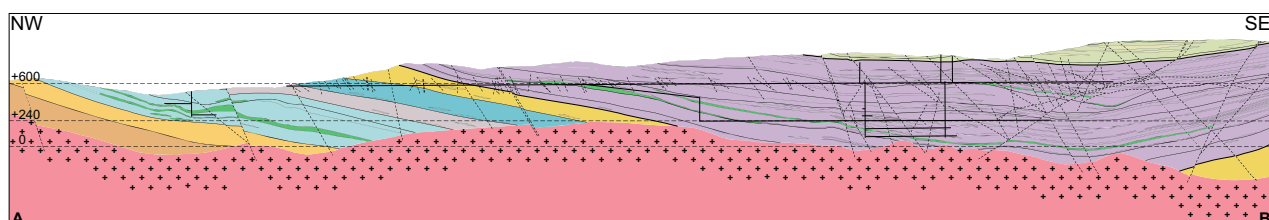


Fig. 2. Longitudinal cross section (refer to Fig. 1 for legend) through the Poehla-Tellerhaeuser Ore Field (modified from Hiller *et al.* 2013).

	Group	Litho-stratigraphic column	Characteristic lithology
Ordovician	Thum Group		Thum Group (1st layer/DEM in 3D model): ≤600 m Upper: phyllitic, often graphitic schist with intercalations of greenschist and quartzite Lower: marble/skarn
	Jáchymov Group		Upper suite (2nd/3rd layer in 3D model): 250 m two-mica- and chlorite schist with intercalated marble/skarn and graphitic schist
			Middle Suite (4th/5th layer in 3D model): 500 m mica schist intercalated with layers/lenses of marble/skarn, quarzitic or graphitic schist, skarnified mica schist, gneiss, and amphibolite
Cambrian			Lower Suite (6th/7th layer in 3D model): 250 m monotonous two-mica- and chlorite-muscovite schist
	Klínovec Group		Fichtelberg Suite (8th layer in 3D model): 200 m mica schist with quartzite intercalations
			Obermittweida Suite (9th layer in 3D model): 350 m metagreywacke and metaconglomerate, two-mica and chlorite schist
			Raschau Suite: >950 m Upper (10th layer in 3D model): gneiss-mica schist Middle (11th layer in 3D model): mica schist, quartzite, amphibolite, and dolomitic marble/skarn horizons Lower (12th layer in 3D model): mica schist

Fig. 3. Litho-stratigraphic column (refer to Fig. 1 for legend) and lithological description of the suites (modified from Hösel 2002; Schuppan & Hiller 2012). The layers in the 3D geologic model define the upper boundary of the suites. Suites Niederschlag Group (13th layer) and Přísečnice Group (14th layer) are not excavated within Poehla-Tellerhaeuser Ore Field, thus are not shown in the litho-stratigraphic column. Some suites are separated according to lithologic changes.

meters length) which were mapped at the 600 masl level at Haemmerlein and Tellerhaeuser during exploration (Fig. 6, V.I. Velichkin & B.P. Vlasov, unpublished report). Most of the drawings show the central element of the faults but not the entire fault zone. Like Kuschka (2002) described for many faults situated in the Ore Mountains, also at Poehla-Tellerhaeuser Ore Field fault zones usually consist of multiple fault planes dividing the fault zone in multiple shear lenses (Fig. 6A,B). This is the result of multiple reactivation and mineralization cycles creating a dense partially mineralized fault network bordering rhomboidal to rectangular blocks (Hiller 1995; Kuschka 2002; Andreani *et al.* 2014; K.P. Stanek, unpublished report). Although many faults exhibit a fault core consisting from gouge and/or fault breccia, displacement indicators are quite rare (Fig. 6). Displacement estimation is therefore difficult. Most of the fault damage zones are (partially) mineralized with different types of quartz, fluorite, iron ores, and dolomite. Accessory mineralizations are barite, calcite, cassiterite, sphalerite, pitchblende, which resulted from contact metamorphic overprint of the underlying late-Variscan granites and subsequent metasomatic and hydrothermal processes. Also processes altering the damage zone and the host rock were identified in most faults, such as metasomatism, greisenization, albitization, sulfidization, and vein-related alteration.

Inflow sampling and database

The uranium ore pitchblende was originally prospected in the Poehla-Tellerhaeuser Ore Field with radon surveys of

groundwater inflows to long exploration drifts down to a depth of 900 mbgs. The Soviet-German stock company Wismut (SDAG Wismut) had a sampling team within the department of hydrogeology measuring and sampling inflows with very high accuracy. Up to six control measurements within weeks, months, and years after excavation are reported whenever high inflow rates or special water compositions were encountered. Data were compiled in sampling books which are stored at the Archive of Wismut GmbH (Table S2). Digitalization of the data was done by the staff members of this archive and the authors. Datasets with this quality and quantity of measurements are unique and provide an extraordinary insight into the hydrology of an ore field.

The complete hydrogeological database which we have created for this project consists of a total of 1141 ‘early time’ preferential groundwater inflows to about 125 km of drifts and 15 km of boreholes (Table S3). The compilation includes location of inflows, flow rates, host rock petrography, mineralogy of the fracture infill, hydrochemical properties, and small-scale structural information of the transmissive features. After excluding measurement locations without inflow, repeat measurements, and discrete inflows whose position is uncertain, a total of 1030 sampling points remained for analysis (Table 2). Therefore, overall roughly every 130 m an inflow was encountered. In comparison, the experimental mining blocks (‘Tin Chambers’) within the Haemmerlein deposit exhibit a mean fracture spacing between 15 and 0.4 m. Common maximum fracture spacings within crystalline rock are in the range of

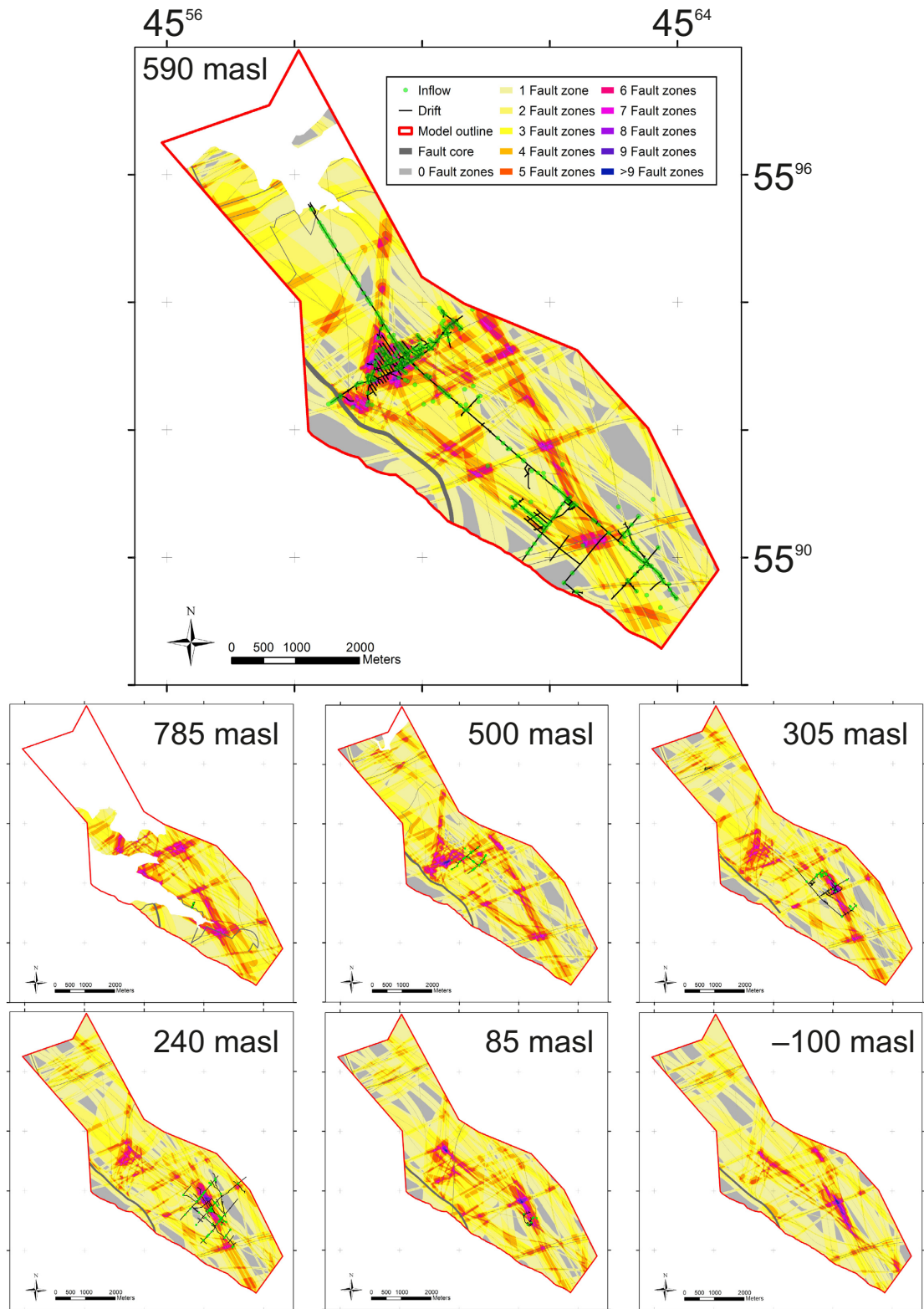


Fig. 4. The fault network, excavations and position of inflows measured are shown at selected elevations. Fault cores are shown in dark gray. Overlapping areas of fault zones are color coded according to the number of overlapping fault zones assuming symmetric fault architecture and constant, depth independent fault zone thickness.

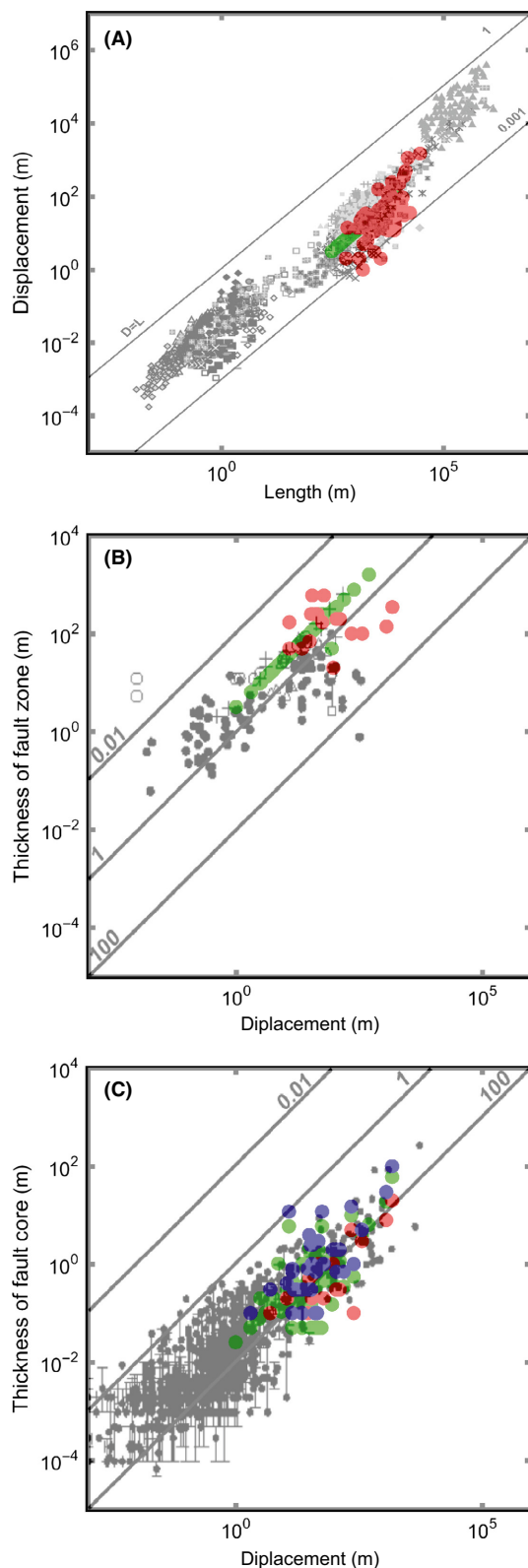


Fig. 5. Structural data compared to datasets compiled by (A) Torabi & Berg (2011), (B) and (C) Childs et al. (2009). Red dots in A and B display data of 131 faults from literature, geologic maps, and cross sections at Poehla-Tellerhaeuser Ore Field (a total of 131 measurements of fault trace length, 68 of fault displacement, 28 of thickness of fault zone, and 92 of the thickness of fault core). Blue dots in C display the upper limit reported for each fault, and red dots display the lower limits. Green dots represent data estimated by the power law relationships established by Kolyukhin & Torabi (2012).

decameters, therefore at least an order of magnitude lower in comparison with spacing of inflows observed here (compare e.g., Talbot & Sirat 2001). The 3D spatial information of inflows is obtained from digitalization of drift maps of the individual levels of the mine. No structural measurements are available at the inflows at Globenstein and only for 35% and 47% of all inflows at Haemmerlein and Tellerhaeuser, respectively (Table 2). The flow rates are taken as representative of structurally induced flow, thanks to the early time measurements and because the tunnels were usually not grouted.

Flow rates in the range of 1.7E-8 to 3.6E-2 m³ sec⁻¹ were measured at Tellerhaeuser and Haemmerlein and 8.3E-7 to 3.7E-2 m³ sec⁻¹ at Globenstein. The lowest limit is assigned to dripping inflows with rates lower than 1.7E-8 m³ sec⁻¹ (corresponding to 1 ml min⁻¹). The distribution of inflow rates is close to log-normal (Fig. 7). For such log-normal shaped flow rate distributions, and as described in Masset & Loew (2010), a few very high inflows typically dominate the total inflow to underground excavations. This is also the case for the Poehla-Tellerhaeuser Ore Field, where the five largest single discrete inflows ($Q > 0.01 \text{ m}^3 \text{ sec}^{-1}$) account for about 35% of the cumulative inflow rate (Fig. 7). As these inflows are important for the overall hydraulic behavior of the mine, they are described in detail in Table 4. Large inflows are spatially distributed all across the Poehla-Tellerhaeuser Ore Field and exhibit no significant relation to factors like lithology and overburden. However, they are all situated in the circumference of one or more faults hosted in mica schists or calcareous rocks.

To validate our inflow dataset, we cumulated the inflow rate for single mining levels and compared those to independently measured maximum pumping rates from these mining levels (Table 3). As inflow rates to deep underground excavation have to decrease with time and inflows often show hydraulic interactions, the cumulated (early time) inflow rate to the individual levels should be higher than the highest pumping rate from these levels as measured during excavation. The comparison of these values as shown in Table 3 can be regarded as a semiquantitative validation of our inflow measurements. Only levels 180 and 85 masl exhibit smaller cumulative early time flow rates than measured. The difference could be partially

Table 1 Compilation of main fault groups, their orientation, structural properties, style, and time of activation as well as time and style of last reactivation (data compiled and generalized from Hiller 1995; Hösel 2002; Schuppan & Hiller 2012; K.P. Stanek, unpublished report).

Group	Strike (°)	Dip (°)	D (m)	DZT (m)	CT (m)	Initial formation	Style	Last reactivations	Style
NW-SE	120–150	50–70 SW (NE)	0–300	<350	–	Upper Carboniferous	SS	Ductile/Brittle	Post-Miocene Tertiary Post-Cretaceous
NE-SW	30–75	40–50 SE	0–20	<30	<5	Lower Carboniferous	SS/NF	Ductile/Brittle	Pliocene but before last reactivation of NNW-SSE striking faults
		60–75 SE	0–20	–	<5	Carboniferous	SS		SS/NF?
		0–20 SE	>km?	<50	<1	Lower Carboniferous	RF	Ductile	'younger movements'
N-S	160–180 0–30	45–80 E/W	<20	<20	<20	Carboniferous and/or Cenozoic	NF/RF?	Brittle	Before most recent reactivation of NW-SE striking faults
W-E	75–100	55–90 S	–	<170	<4	Upper Carboniferous	–	Brittle	Post 30 Ma partially before last reactivation of NW-SE striking faults
NNW-SSE	150–160	70–90 ENE/(WSW)	<2	<50	<2	–	–	–	SS

D, displacement; DZT, fault damage zone thickness; CT, fault core thickness; SS, strike-slip fault; RF, reverse fault; NF, normal fault; ?, unsure; –, unknown.

attributed to process (drilling) water pumped into the mine, which becomes an important contributions, when the tunnel inflows are small. Overall, it is believed that most of the discrete inflows to the tunnels were measured accurately and completely.

Dissolution and paleo-karstification

One significant inflow at Globenstein is unequivocally related to a larger karst dissolution cavity ('unregistered' in Table 4) with a dimension of 2 × 3 × 15 m (Hösel 2002). Based on this geologic observation at the Globenstein deposit and the fast decrease of inflow rate, the geologist claimed that high water inflows at the Tellerhaeuser deposit at level 300 masl (sample numbers 300017 and 300028) are also related to paleo-karst structures (Schuppan & Hiller 2012). A total of 25 inflows are situated within this area. In addition, a total of 70 minor inflows are situated within fractured marble and cataclastic marble at the level 350 masl (plus 1 inflow at the level 410 masl) in the Globenstein deposit and might be a result of minor karstic dissolution along fractures. As it can be shown that karstic features and respective inflows in the Poehla-Tellerhaeuser Ore Field are usually associated with faults, inflows possibly fed from dissolution features remained in the database used for further analysis.

Mesoscale fracture properties at inflow locations

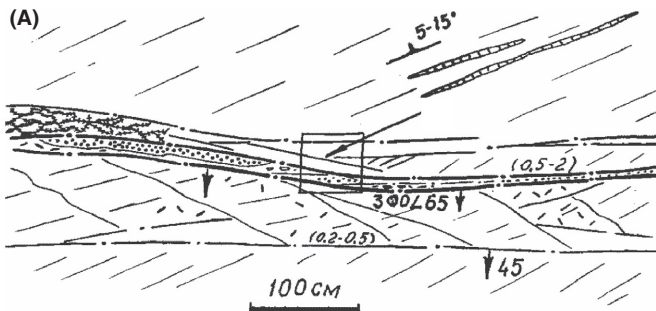
Most preferential inflows are related to faults or joints. For 30% of these, a thickness of the transmissive structure (ranging between 0.4 and 150 cm) has been reported (Table 2). While larger faults usually were created naturally, smaller fissures or joints without infill might also be the result of excavation. As the mechanism

of creation and the persistence of these conduits is often not known, we will further refer to them as mesoscale fractures. Conductive mesoscale fractures show a large variation in spatial orientation, with a dominance of NW-SE oriented and rather steeply (>45°) SW dipping orientations (Fig. 8A). Half of the inflow rate to the drifts is derived from NW-SE striking mesoscale fractures (Table 5) while the other half is equally distributed within the other main orientations (10–17% each). Partially, this trend is biased as orientation of the mesoscale fractures was not measured within the deposit Globenstein. We did not encounter a direct relationship between the thickness of transmissive structures, their orientation, and the flow rate.

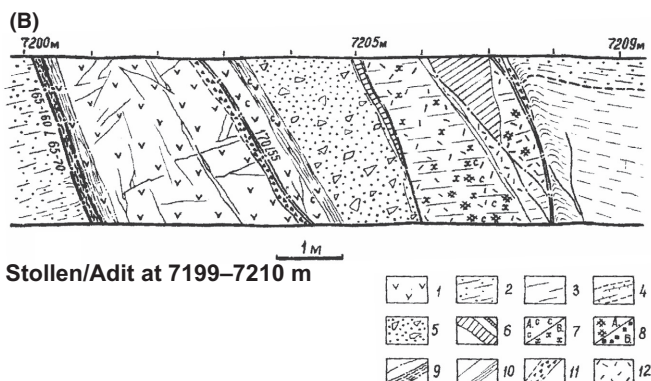
DATA PREPARATION AND PROCESSING

GoCad model boundaries and workflow

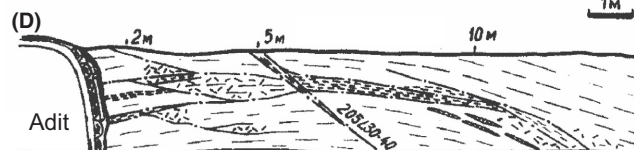
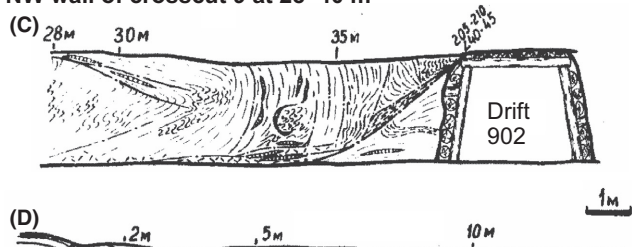
Preferential groundwater inflows, faults, and litho-stratigraphic units have been integrated into a 3D geological model using the code SKUA-GOCAD. The type of data, data description, and data sources used for the 3D geological model are compiled in Table S2. The model of Poehla-Tellerhaeuser Ore Field is based on geologic surface maps (4) and geologic mining plans (11) as well as cross sections (Figure S1A). Geological sections roughly trend NW-SE (5) and NE-SW to W-E (10) crossing the main axis of the mine in the depth range between –500 and 900 masl (Figure S1B). Usually, both the geologic (level) maps and the cross sections exhibit litho-stratigraphic units and fault traces. The information was cross-checked against additional sources, such as regional structural maps. The surface of the underlying granites is modeled using elevation maps from the greater mining area of Schlema-Alberoda and Poehla-Tellerhaeuser Ore



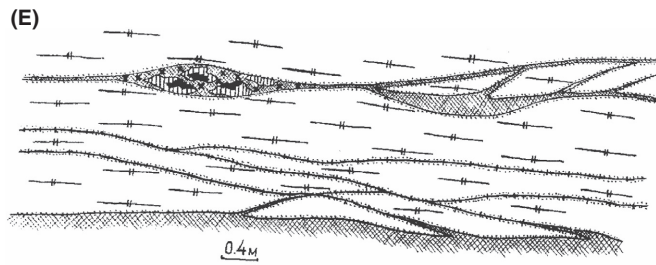
Roof of drift 112b at 155–165 m



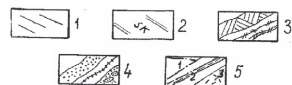
NW wall of crosscut 9 at 28–40 m



SE wall of crosscut 10 at 0–14 m



NW wall of crosscut 2 at 181–188 m

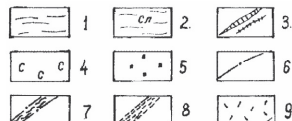


Architecture of a NW-SE striking fault in quartzitic schists and skarnes at deposit Haemmerlein

- 1- Quartzitic schist
- 2- Skarne
- 3- Dolomite with comb quartzitic selvedge
- 4- Milky quartz
- 5.1- Tectonic fractures
- 5.2- Sheet vein
- 5.3- Intensively fractured rock

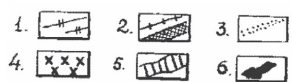
Architecture of large NE-SW striking faults at deposit Tellerhaeuser

- 1- Phonolite Dyke
- 2- Bright quartzitic mica-schist with feldspar
- 3- Dark schist
- 4- Fractures with skarn
- 5- Silicified breccia
- 6- Quartz veins
- 7- Hydrothermally bleached rock/chloritization
- 8- Fissures with calcite/pyrite
- 9- Tectonic fractures
- 10- Fissures with foliation
- 11- Tectonic breccia
- 12- Intensively fractured rock



Architecture of N-S striking faults in carboniferous schist at deposit Tellerhaeuser

- 1- Carboniferous mica-schist
- 2- Bright quartzitic mica-schist with feldspar
- 3- Quartz veins
- 4- Argillitization
- 5- Sericitization
- 6- Fault with slickensides
- 7- Gouge
- 8- small-scale shear zones
- 9- Intensively fractured rock



Architecture of bedding parallel fractures in muscovitic gneisses at deposit Haemmerlein

- 1- Muscovitic gneiss
- 2- Amphibolites and amphibolitic veins
- 3- Albitization
- 4- Chloritization
- 5- Milky quartz
- 6- Coarse grained cassiterite

Fig. 6. Examples of the fault zone architecture at the 600 masl level at the Haemmerlein and Tellerhaeuser deposits. (A) Plain view onto a NW-SE striking fault with typical shear lense architecture. (B) NE-SW striking fault which was reactivated multiple times and therefore consists of multiple fault planes. (C) 'Young' N-S striking fault with single fault plane surrounded by drag folds. (D) 'Young' N-S striking fault with slickensides. (E) Bedding parallel thrust faults showing amphibolitic overprint (compiled from V.I. Velichkin & B.P. Vlasov, unpublished report).

Table 2 Reported inflow sampling locations, parameters, and distribution of the measurements within the entire dataset and the subdatasets.

	Globenstein	Haemmerlein	Tellerhaeuser	Ore Field
Total number of sampling locations	213	453	364	1030
Spatial information	213	453	364	1030
Inflow rate	213	453	364	1030
Strike/Dip of transmissive fracture	0	213	128	341
Thickness of transmissive structure	0	210	119	329
Altered/strained rock mass	84	69	17	170
Cataclastic rocks	0	16	23	39

Field. The geologic special maps (field maps) of Breitenbrunn, Erla, and Zweibach are used for the surrounding area of the mine.

The 3D model roughly follows the surface outline of the Poehla-Tellerhaeuser Ore Field stretching over an area of about 14×4 km in NW-SE and NE-SW direction (Fig. 1). The surface topography has been derived from a 2 m-DEM of Saxony which was upscaled to 10 m forming the upper model boundary, and the bottom boundary is set to -100 masl. The faults, litho-stratigraphic, and lithological surfaces are modeled by fitting traces on the cross sections and geologic maps with a discrete smooth interpolation algorithm partially embedded in the Structural Modeling Workflow (Figure S1C–E). Faults are usually based on at least two individual traces derived from different level maps and/or cross sections. Occasionally, faults are modeled with one trace wherever gaps in the structural framework are encountered. The dip of those faults is inferred from neighboring faults. Such badly constrained faults only amount to about 10% of the total number of faults and are situated on the edges of the model and

between the deposits Globenstein and Haemmerlein. A total of 131 faults are modeled (Figure S1F), of which 31 faults exhibit a displacement of 10 m or more (Figure S1G). These faults with larger offsets define the compartmentalization of the 14 modeled litho-stratigraphical units (Fig. 3 and Figure S1H).

Calculation and distribution of discrete inflow transmissivities

The transmissivities of conductive mesoscale fractures drained by the mine are estimated from the simplified analytical solution of Jacob & Lohman (1952):

$$\frac{\Delta h}{Q(t)} = \frac{2.3}{4\pi * T} \log\left(\frac{2.25 T * t}{r^2 S}\right) \quad (1)$$

where Δh is the hydraulic head drawdown (m), $Q(t)$ is the measured flow rate ($m^3 sec^{-1}$), T is the transmissivity ($m^2 sec^{-1}$), r is the radius of the well or drift (m) and S is the storativity (–). The basic assumptions are confined radial Darcy flow to a circular well or drift with constant drawdown (governed by the atmospheric pressure conditions in the open drift). 2D radial flow is a good approximation for flow from a single persistent fracture oriented at a large angle with the axis of a linear underground excavation.

As the inflow measurements were usually conducted shortly after excavation of exploratory drifts into virgin ground, an initially undisturbed hydraulic head field is assumed based on a topographic control of the hydrostatic pressure conditions. The groundwater table is assumed to be near ground surface, which is in good agreement with the observed water tables usually found 2–15 mbgs (Schuppan & Hiller 2012). An underestimation of transmissivity resulting from the long-lasting excavation process in the mines, and ore fields are prevented by careful selection of (mainly reconnaissance) drifts. Nevertheless, the excavation scheme suggests that

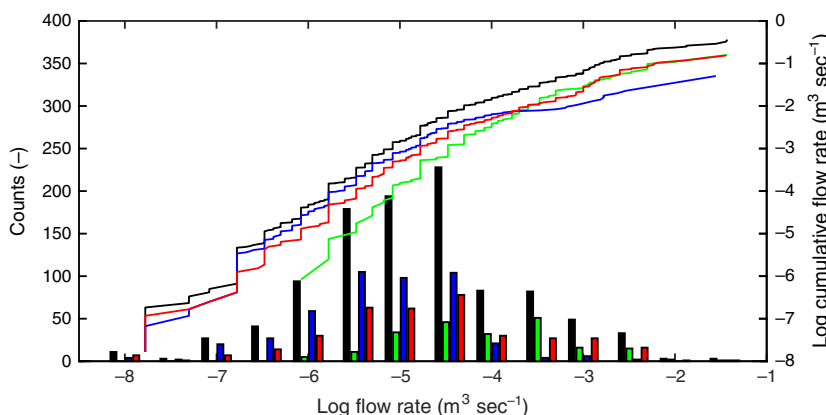


Fig. 7. Histograms of inflow rates (column) and cumulative flow rates (graphs) for the entire dataset (black) and the subdatasets Globenstein (green), Haemmerlein (blue), and Tellerhaeuser (red).

flow rates may be underestimated at intermediate levels between the reconnaissance and active mining levels (levels 300 & 180 masl).

Storativity of the rock mass in the Ore Mountains is poorly known. The storativity is set to 1E-5 m/m which is the average experimentally estimated value for fracture zones in granites at the Grimsel Test Site situated in the Swiss Alps (Guyonnet & Lavanchy 1992; S. Loew & O. Masset, unpublished report).

The delay between the time of inflow measurement and the excavation of individual inflows is estimated based on the excavation progress documented on the plain views of the mine levels. The delay ranges between some days to 3 weeks; an average time of 2 weeks was used for most calculations. Inflows from boreholes were measured during drilling, and we estimated that measurements were taken

Table 3 Comparison of cumulative early time flow rates to mine levels and highest measured pumping rates from the same mine levels (yearly averages).

Deposit	Mine level	Cumulative flow rate measured [†] (m ³ h ⁻¹)	Cumulative early time inflow rates
Haemmerlein/ Tellerhaeuser	+610, +585/600, +530,+500 masl	75.2	203.4
Tellerhaeuser	+300 masl	40.6	326.8
	+240 masl	57.6	94.8
	+180 masl	6.6	2.3
	+120 masl	30.3	108.4
	+85 masl	13.1	3.4
Globenstein	Entire deposit	120.0*	570.0

*Only reported value from Hösel (2002). †From Schuppan & Hiller (2012).

Table 4 Inflows with high inflow rates.

Sample number	Date	Deposit	Level (masl)	Over-burden (mbgbs)	Location	TM/DM (m)	Flow rate (m ³ sec ⁻¹)	Litho-stratigraphy	Structure	Azimuth/ Dip (°)	Distance (m)
410018	05.1975	Globenstein	410	224	Qu. 18N	90	0.037	Lower Raschau	3 unnamed faults	~245/85 ~245/30 ~90 or 270/-	5 20 15
350010	10.1984	Globenstein	350	156	Str. 103b (D)	–	0.013	Lower Raschau	Globenstein fault	135/51	5
Unregistered*	–	Globenstein	350	–	Str. 20	–	0.022	Lower Raschau	–	–	–
600217	04.1970	Haemmerlein	600	217	Qu. 1 (D)	187	0.028	Middle Jáchymov	Unnamed fault	–	15
300017	01.1988	Tellerhaeuser	300	628	Fe. 8903	97	0.036	Upper Jáchymov	Luchsbach faults	~221/53	–
300028	02.1988	Tellerhaeuser	300	607	Fe. 8903 (D)	42	0.013	Upper Jáchymov	Kunnersbach faults	~62/75	–
								Luchsbach faults	~221/53	–	
								Kunnersbach faults	~62/75	–	

D, drilling; TM/DM, tunnel meter/drilling meter; Qu./Fe., crosscut; Str., drift; –, unknown. *Reported by Hösel (2002).

up to 1 h after drilling through the water bearing zones. For the detailed procedure and the discussion of critical parameters, please refer to Masset & Loew (2010, 2013). The distribution of transmissivities obtained from all inflows is shown in Fig. 9.

Structural properties of modeled fault zones

As shown in Fig. 8 and Table 5, modeled faults are mainly striking NW-SE dipping to the SW and NE-SW dipping to the SE. Dip angles are usually fairly steep, mainly ranging between 45° and 90°. Due to the NW-SE elongated model area, NW-SE striking faults are under-represented in number but overrepresented in total fault length—the relationship is vice versa for NE-SW striking faults (Table 5). NNW-SSE, N-S, and W-E striking faults are of minor importance. Structural properties of these fault groups are rather uniformly distributed.

A total of nine cross sections perpendicular to the main orientations of the faults are sampled from the 3D model for spacing analyses. Each cross section only takes into account the spacing between faults of the same orientation group, and each group is represented by 6.6–11.2 km total sampling length. Table 6 shows that average values of fault spacing increase with depth, for example, the median values nearly double from about 250 to 430 m within the elevation interval of 700–200 masl.

The hydraulic behavior of fault zones is strongly dependent on the geometrical properties of fault core and damage zones. Therefore, fault displacements, length, and thickness are compiled from Schuppan & Hiller (2012) and Hösel (2002), the geologic surface maps, and the

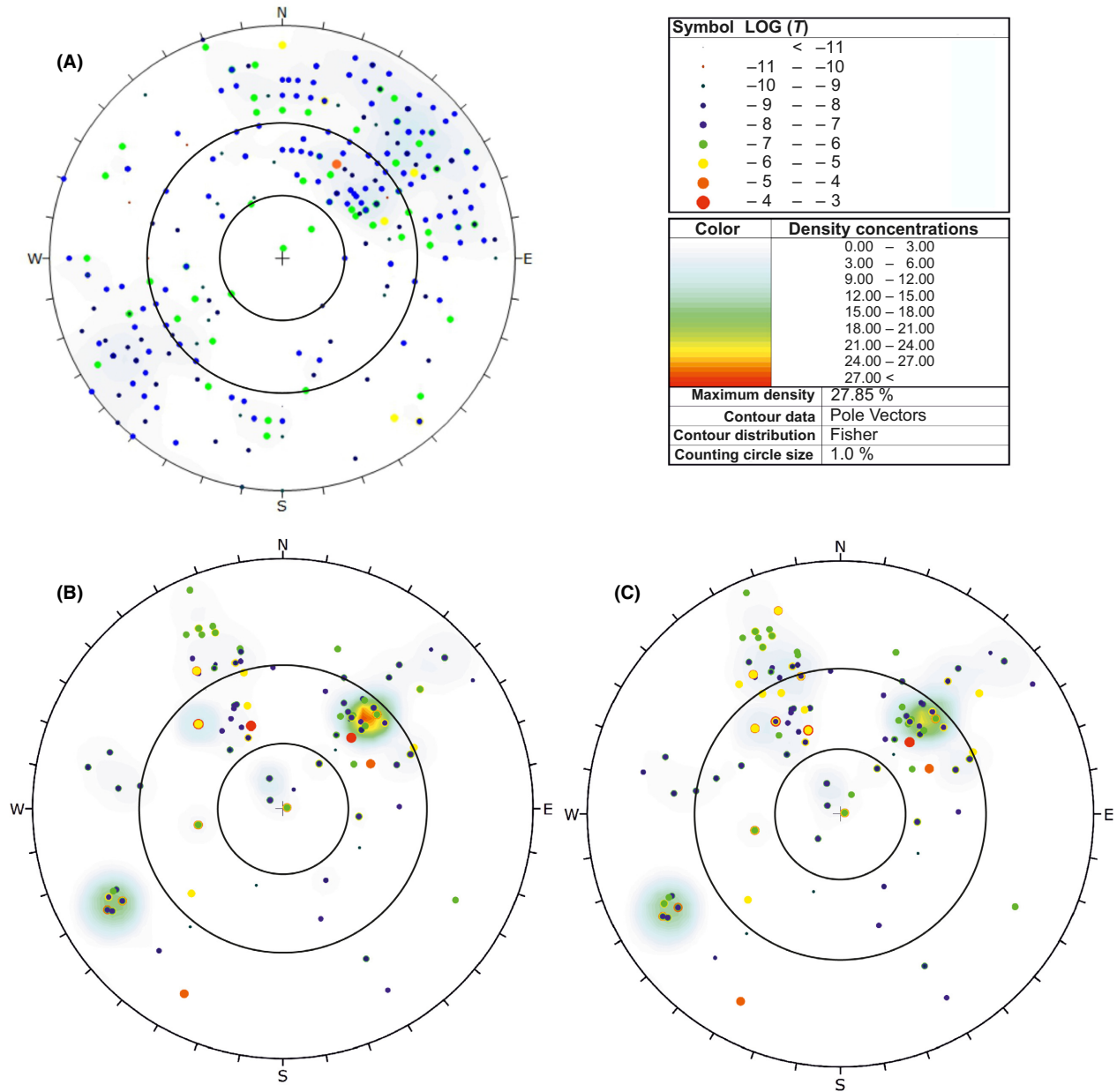


Fig. 8. Poles to fault planes (lower hemisphere) and density contours (Fisher distribution) of (A) transmissive mesoscale fractures, (B) transmissive mining scale faults determined by the RCFD approach, (C) transmissive mining scale faults determined by the ACFD approach. The poles to fault planes are color coded according to the decimal logarithm of the transmissivity. Scaling circles are situated at dips of 30°, 60°, and 90°. Densities represent orientation densities. Note that multiple discrete inflows may be situated at the same pole.

geologic 3D model of Poehla-Tellerhaeuser Ore Field (Figs 5 and 10). These fault properties are mainly available for the NW-SE, NNW-SSE, and N-S striking faults. The fault trace length is calculated from the edge points of the modeled faults if no other description is available. The trace length is generally well estimated for most of the faults. Only for five NE-SW striking faults (four of which situated close to inflows), the length might be underestimated because of truncation by the 3D model boundaries.

A geometric mean of vertical and horizontal displacements is used to calculate the displacement vector length. The resulting structural properties are in agreement with previous statistical relationships derived by Torabi & Berg (2011) and Childs *et al.* (2009); see Fig. 5 blue and red dots.

For faults where only length but not displacement and thickness data are available, we use the power law statistical relations derived by Kolyukhin & Torabi (2012) for

Table 5 Distribution of strike directions of conductive mesoscale fractures (inflows) and correlated faults (inflows without information are excluded so that the sum of the fractions yields one).

Dip direction	Strike direction	Fraction of number of faults	Fraction of fault trace length in the 3D model	Fraction of single inflows associated with			Fraction of cumulative inflow rate generated within the orientation class of		
				Mesoscale transmissive fractures	ACFD		Mesoscale transmissive fractures	ACFD	
					RCFD	RCFD		ACFD	RCFD
NE (SW)	120–150°	0.31	0.41	0.38	0.44	0.47	0.44	0.46	0.45
WSW (ENE)	150–160°	0.07	0.09	0.13	0.13	0.13	0.14	0.18	0.18
W & E	160–180° & 0–30°	0.12	0.12	0.19	0.09	0.10	0.17	0.03	0.03
NW (SE)	30–75°	0.42	0.30	0.10	0.31	0.27	0.11	0.33	0.34
N	75–100°	0.04	0.05	0.10	0.02	0.01	0.10	0.00	0.00
Others	100–120°	0.04	0.03	0.10	0.01	0.02	0.04	0.00	0.00

Highest fractions of each parameter are shown bold.

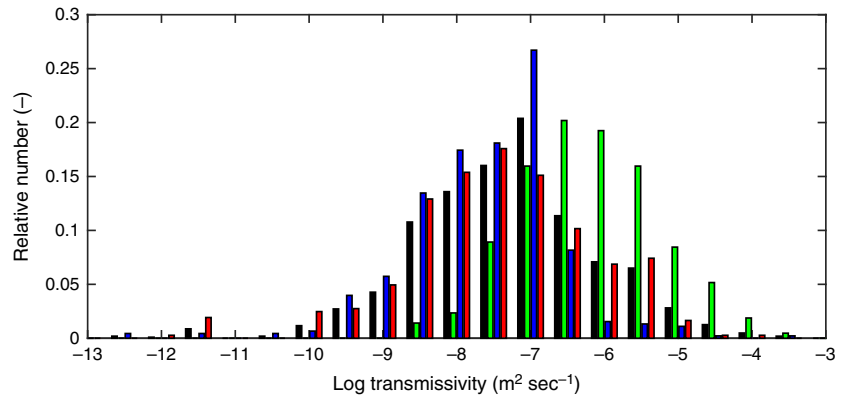


Fig. 9. Histograms of the distribution of the logarithm of mesoscale fracture transmissivity for the entire dataset (black) and the sub-datasets Globenstein (green), Haemmerlein (blue), and Tellerhaeuser (red).

Table 6 Values of the descriptive statistics of the fault spacing in comparison with geodetic elevation.

Geodetic elevation (masl)	100	200	300	400	500	600	700
Harm. Mean (m)	125	92	57	79	61	83	24
Geom. Mean (m)	336	307	254	267	264	247	235
Arith. Mean (m)	787	733	685	655	707	706	644
Median (m)	354	428	260	319	294	232	255
5%-Quantile (m)	27	25	16	34	18	19	15
95%-Quantile (m)	3802	2942	2851	2460	3160	3264	2518

estimation of fault displacement and core thickness (green dots in Fig. 5). For the estimation of displacement D (m), the following relationships for strike-slip faults are used:

$$D = \begin{cases} 10^{1.031 * \log(\frac{L}{100})}, & D < 1540 \text{ m} \\ 10^{2.041 * \log(\frac{L}{100})}, & D > 1540 \text{ m} \end{cases} \quad (2)$$

where L is the fault trace length (m). The fault zone thickness FT (m) is calculated from:

$$FT = 3.200 * D \quad (3)$$

and the fault core thickness CT (m) from:

$$CT = \begin{cases} 0.0256 * D, & CT < 0.09 \text{ m} \\ 0.0128 * D, & CT > 0.09 \text{ m} \end{cases} \quad (4)$$

Fault zone coverage is calculated for the mining levels assuming symmetric architecture and constant fault zone thickness within the individual fault zone (Fig. 4). The area covered by high numbers of fault zones retraces the major faults identified. A decreasing percentage of overlapping fault zones is observed with increasing depth, showing that destruction at the surface is more intensive than in the underground. Simultaneously, the area not covered by any fault remains constant at around 10% yielding evidence that surficial destruction is focused to the existing damage zones of the large-scale faults. The fault core yields about 0% to 17% of the single fault zone thickness which results to about 2.1% of the total area of the single levels at 715 masl and decreases constantly to about 1.6% of the total area at -100 masl.

Correlation between inflows and fault zones

To study the relationships between small-scale preferential groundwater pathways and the surrounding faults zones—

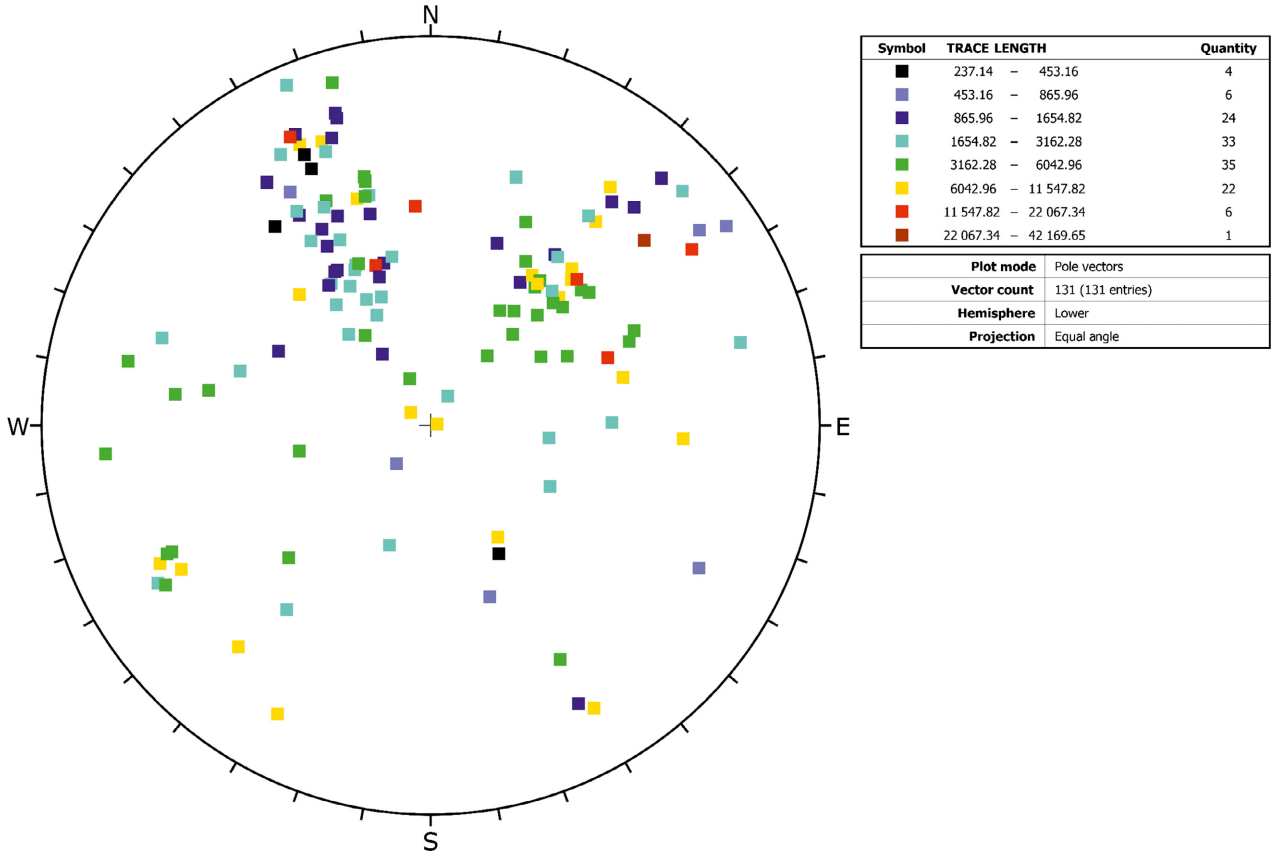


Fig. 10. The poles of the faults are plotted within the lower hemisphere. The poles are color coded logarithmically according to the trace length of the faults.

that is, the hydraulic architecture of the large modeled faults—the individual inflows from mesoscale fractures are spatially related to the individual fault zones using the closest distance to the fault center. This was done for two different distance metrics calculated in 3D space between the inflow points and the mesh points of the modeled faults:

- (1) Absolutely closest fault distance (ACFD): The orthogonal distance between the inflow point and each modeled fault is approximated by the minimum distance between the inflow point and the mesh points of the fault center of all faults (Fig. 11). The smallest value represents the absolutely closest fault (ACFD).
- (2) Relatively closest fault distance (RCFD): The orthogonal distance between the inflow point and the modeled faults is approximated by the minimum distance between the inflow point and the mesh points of the fault center of all faults. Each distance between the inflow point and the faults is normalized by the fault zone radius (half-thickness) of the respective fault. RCFD is the distance to the fault with the lowest percentage of all normalized distances (Fig. 11).

As a result, we are able to relate each inflow point to fault properties like fault orientation, length or thickness. Each inflow can be spatially related to one or two possible faults

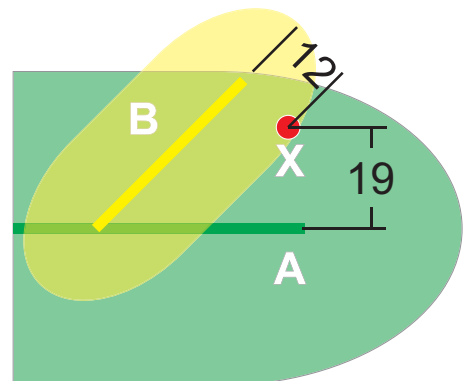


Fig. 11. A generic plain view onto two faults and their fault zone thickness is displayed. For reason of clarity, a linear scaling between fault trace length and fault zone thickness is used in this figure as with the logarithmic relation (Eqs 2 and 3) the smaller fault zone thickness is not possible to display. A major fault zone A (green) exhibits a fault zone radius of about 30 units and a smaller fault zone B (yellow) exhibits a fault zone radius of about 15 units. Fault B is the absolutely closest fault (ACFD) 12 units away from the inflow point X (red dot). This distance equals to a relative distance of 80% within the fault zone radius of Fault B. In comparison, the inflow X is situated at an absolute distance of 19 units which equals to about 65% of relative distance within fault zone radius of Fault A. Therefore, Fault A is called the relatively closest fault (RCFD).

when considering the two distance metrics (ACFD and RCFD might also be the same distance to the same fault).

RESULTS

Mesoscale fracture transmissivity

The transmissivity values, as derived from inflows to the single deposits of the Poehla-Tellerhaeuser Ore Field, are close to log-normal distribution (Fig. 9) supporting the selected analysis approach. The distribution of log transmissivity at the Globenstein deposit is symmetric and clearly shows the highest median and geometric mean values. This is most probably due to the shallow depth of the excavations below ground surface at Globenstein and possibly also to the fault orientation of conductive faults as discussed in later sections (Fig. 12). The orientations of mesoscale conductive fractures in the entire Poehla-Tellerhaeuser Ore Field are strongly dispersed, but highly transmissive fractures preferably dip toward SW (Fig. 8A). This strong dispersion might also be affected by excavation induced fracturing and stress redistribution around the excavations.

Groundwater flow within mining scale fault zones

Based on the processing described above, most of the 1030 mine inflows—except 33 inflows—are located in at least one fault damage zone. Single inflows (representing preferential groundwater pathways) are spatially attributed to up to 10 faults, whereas more than half of the total inflow rate comes from inflows which are attributed to four to six fault zones (Table 7). This implies that the main portion of the preferential groundwater pathways and of the groundwater flow predominantly occurs within the overlap area of multiple fault damage zones (Fig. 4). The distribution of transmissivities of inflows located within a

Table 7 Mean $\log T$ and test statistics of the Kolmogorov–Smirnov Tests on a 5% significance level of the transmissivities derived from single inflows draining a certain number of fault zones. P -values below 0.05 indicate rejection of the null hypothesis of the data being derived from the same continuous distribution.

	Number of drained fault zones				
	0	1–2	3–4	5–6	>6
Number of observations	32	327	359	251	60
Mean $\log T$	−7.67	−7.00	−7.30	−7.51	−7.81
Number of drained fault zones					
0	1	0.026	0.079	0.682	0.243
1–2		1	0.011	<0.001	<0.001
3–4			1	<0.001	<0.001
5–6				1	0.049
>6					1

specific number of fault zones is shown in Fig. 13. Based on the nonparametric Kolmogorov–Smirnov Test (Massey 1951; Lilliefors 1967), the distribution of the transmissivities within pairwise grouped fault zones is mostly dissimilar between the fault groups, and therefore, differences in the mean $\log T$ of the groups are significant (Table 7). Log mean transmissivities increase from inflows not assigned to any fault zone to inflows draining up to two fault zones. With further increase of the number of fault zones drained by a single inflow the mean $\log T$ slightly decreases, reaching a minimum within the group of more than six faults drained by a single inflow. About a third of the 33 inflows not assigned to any fault zone in the geological model are situated close to the model boundary and therefore might belong to fault zones not covered by the model. The resulting mean $\log T$ of this subset might not represent the matrix. The analyses further reveal that the flow rate of single inflows, and hence, its transmissivity is not correlated with the associated fault zone thickness, and in particular

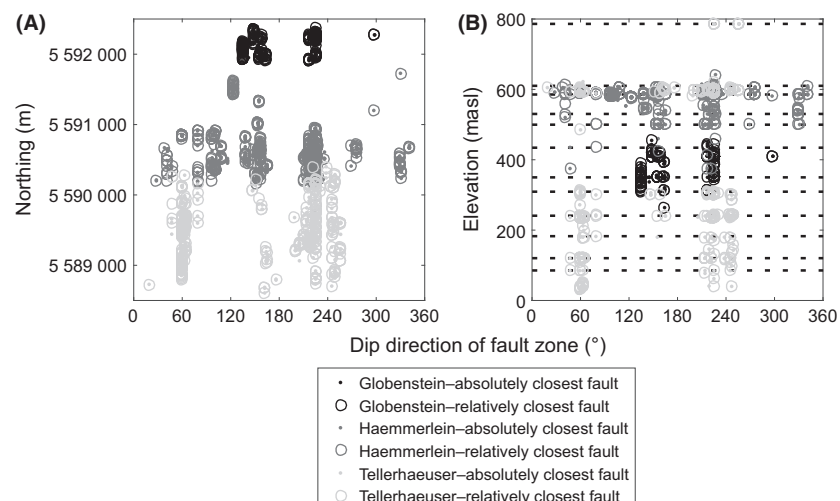


Fig. 12. The dip direction of conductive fault zones derived from ACFD and RCFD is shown (A) versus northing and (B) versus elevation. Dots display the fault dip direction related from ACFD and open circles the fault dip direction related from RCFD. The dashed lines represent the mine levels.

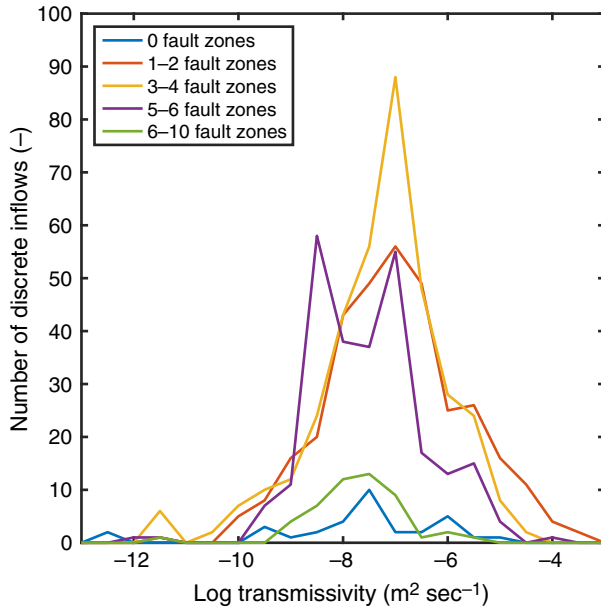


Fig. 13. Comparison of the distribution of inflow transmissivities draining a number of fault zones.

the highest single inflow rates are not associated with the widest fault zones.

The location of an inflow within a fault zone is defined by the relative distances to the fault core considering the fault zone thickness as described above. In addition, cumulative inflow rates are derived from their relative position within a fault zone, starting with 0% cumulative flow rate at the protolith boundary. Such cumulative flow rate distributions within fault damage zones and fault cores are shown in Fig. 14A,B for the two measures of fault distance ACFD and RCFD. The gradient of the cumulative graphs continuously increases from the protolith (relative position 1) toward the fault center (relative position 0) for the deposits indicating a nonuniform hydraulic conductivity distribution. At the Globenstein deposit, the inflows tend to stabilize at around 30% relative distance from the fault center, that is, showing only minor additional inflows in this section which might also correspond to a low permeability fault core. The graphs of Tellerhaeuser and Haemmerlein deposits reach a stable plateau at a relative distance of 0.2–5%. The results from cumulative flow rate curves derived from ACFD and RCFD distances show an overall agreement, although the onset of flow is earlier when using the ACFD distance at Globenstein deposit. In general,

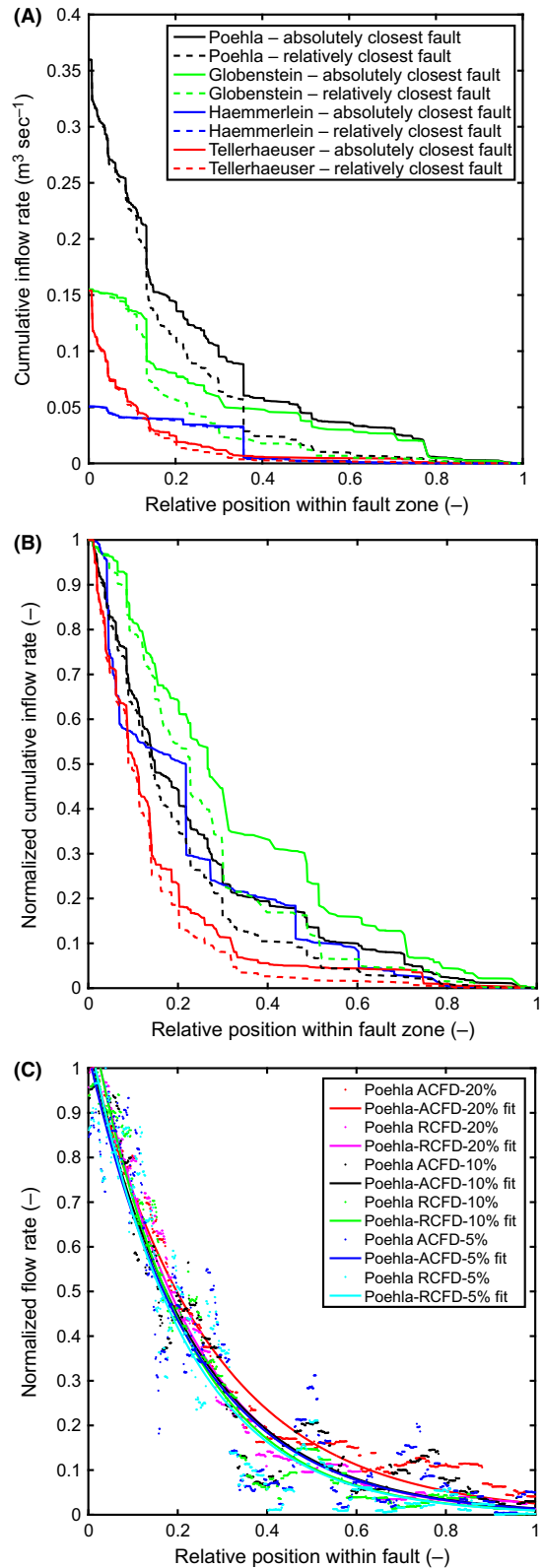


Fig. 14. (A) Cumulative inflow rates from the protolith ($x = 1.0$) to the fault center ($x = 0$) of inflows related by ACFD and RCFD. (B) Normalized cumulative inflow rates without major inflows ($Q > 0.01 \text{ m}^3 \text{ sec}^{-1}$). (C) Moving average of 20%, 10%, and 5% relative fault zone thickness of normalized inflow rates without major inflows ($Q > 0.01 \text{ m}^3 \text{ sec}^{-1}$) of the Poehla-Tellerhaeuser dataset and according fits.

most inflows (and their transmissivity) occur within about a distance of up to 50% of the total fault zone half-thickness as measured from the fault center. Peaks in the overall smooth graphs indicated single large inflows (Table 4) which appear randomly distributed within the fault zones. The inflows with rates larger than $0.01 \text{ m}^3 \text{ sec}^{-1}$ are excluded, and cumulative flow rates are normalized to the total cumulative flow rate of each (sub) dataset in Fig. 14B for comparison reason. The graphs of all deposits exhibit a similar shape of a negative exponential function differing only in the curvature. Spatial derivatives of the normalized cumulative inflow rate for the entire dataset are shown in Fig. 14C using moving average windows of 5%, 10%, and 20% of the fault zone thickness. The exponential fitting equations show a high goodness of fit exhibiting only minor differences in the exponential coefficients for the relational models (ACFD and RCFD) and the averaging distances (Table 8). The graphs for the individual deposits are not shown due to high scatter of the spatial derivatives resulting from fewer data.

Differences in the cumulative flow behavior, such as the onset of flow, the gradient of increase and the difference in curvature of the normalized graphs might be related to differences of the structural inventory. To further explore this topic, we calculated the cumulative flow rates for the different main strike directions (Fig. 15). To assess the entire fault network, also gently dipping faults ($<30^\circ$) are included in the respective fault strike groups knowing that they might be of ductile nature and therefore exhibit different hydraulic behavior. The onset of significant inflow shows remarkable differences between NW-SE and NE-SW striking faults in comparison with NNW-SSE and N-S striking faults. As there are only few inflows assigned to W-E striking faults, the cumulative flow rate graph is not shown.

Spatial orientation of transmissive fault zones and mesoscale fractures

According to Fig. 8B,C and Table 5, the largest contribution to cumulative flow rate is generated within NW-SE

Table 8 Factors and goodness of fit of normalized flow rates versus normalized position of the inflow in a standard fault zone at Poehla-Tellerhaeuser Ore Field following the equation $Q = A \cdot \text{Exp}(B \cdot x)$.

Model	Moving average window (%)	Factor A with 95% confidence bounds	Factor B with 95% confidence bounds	R^2	Standard error
ACFD	5	1.03 ± 0.02	-4.31 ± 0.15	0.89	0.09
	10	1.05 ± 0.02	-4.29 ± 0.10	0.94	0.06
	20	1.05 ± 0.01	-3.72 ± 0.06	0.97	0.04
RCFD	5	1.08 ± 0.02	-4.72 ± 0.13	0.93	0.08
	10	1.14 ± 0.02	-4.75 ± 0.09	0.97	0.05
	20	1.13 ± 0.01	-4.46 ± 0.06	0.99	0.03

and NE-SW striking faults totally resulting in about 79% of the cumulative flow rate. The range of transmissivities associated with the same fault orientations expresses a high degree of hydraulic variability within these faults. The statistical difference of orientation of transmissive faults derived from ACFD and RCFD distance model is only about $\pm 10^\circ$ for both azimuth and dip if the entire dataset is analyzed (Fig. 8B,C).

The orientation of transmissive faults is clearly changing from the NW of the investigation area to the SE (Fig. 12A). The distribution of transmissive faults at the Globenstein deposit is bimodal with preferential dip to the SE and SW. The faults at the Tellerhaeuser deposit dip to the SW, NW, and to a minor extend to WSW and SE. The distribution of transmissive faults at the Haemmerlein deposit is in transition and strongly clustered combining the orientations of the deposits Globenstein and Tellerhaeuser and adding an E dipping cluster. Besides, a regional difference in orientation clustering, also a clear depth-dependent trend is observed for the single deposits (compare Figs 4 and 12). Conductive fault orientations spread all over and do not cluster in the uppermost 200 mbgs (500–600 masl). The conductive faults excavated in the Tellerhaeuser deposit cluster below an elevation of about 300 masl (about 400 mbgs). The higher transmissivities at dip directions of 130° to 140° within the deposit Globenstein might be a result of karstification as inflows related to marble lenses mainly drain these fault zone orientations (Fig. 8).

Gently dipping faults ($<30^\circ$) are mainly situated within the Haemmerlein deposit. For geometrical reason, these seven fault zones include a major portion of the investigated volume and therefore relate to about 10% of the single inflows by both ACFD and RCFD but exhibit only about 0.4% of cumulative flow rate (Fig. 8). As these faults are believed to be old metamorphic (ductile) thrust faults, hydraulic conductivity is expected to be low (Lützenkirchen 2002; Masset & Loew 2010).

DISCUSSION

Uncertainty of 3D fault zone model

The geologic 3D model is based on cross sections and geologic maps from the surface and different mine levels. The horizontal uncertainty of fault positions is approximately 15–25 m in the excavated parts of the mine and—due to map inconsistencies—about 100 m at topographic surface. The latter is of minor importance as inflows were measured in the excavated parts only. Inflows have an uncertainty in positioning of about 5 m. The ACFD and RCFD are calculated using point-to-point distances which is an approximation for the true orthogonal distance between faults and inflows. As a mesh with a point spacing

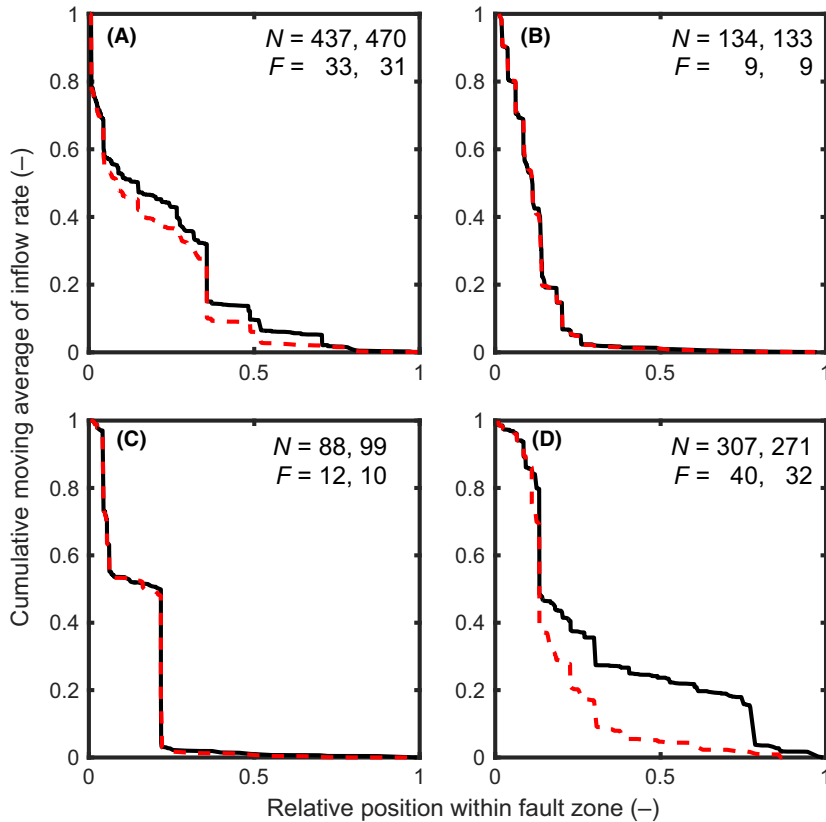


Fig. 15. Normalized cumulative inflow rates for single main strike directions. (A) NW-SE, (B) NNW-SSE, (C) N-S, (D) NE-SW. The number of inflows (N) assigned to each fault group and the number of faults (F) with assigned inflows are shown whereas the first number stands for the number of inflows related by ACFD and the second number for the inflows related by RCFD.

in the meter range (close to the drifts and increasing away from them) is used, the error is below the uncertainty of the inflow and fault positions.

The ratios of measured geometric fault zone properties within the Poehla-Tellerhaeuser Ore Field are consistent with previous investigations (Childs *et al.* 2009; Torabi & Berg 2011). The traces of NE-SW striking faults are shorter and hence show fewer displacement and smaller damage zones (Fig. 10). The high density of relatively large fault zones reflects the repeated faulting activity in this region (Fig. 4) which might have caused increasing connectivity of single small fault planes to larger scale faults and thus increased the fault zone coverage and damage around these faults (Beaudoin *et al.* 2006; Faulkner *et al.* 2006, 2010). Fracture creation is most effective close to the surface due to stress release effects and chemical alteration (Maréchal *et al.* 2004; Lachassagne *et al.* 2011; Roques *et al.* 2014; Welch & Allen 2014) and seems to be focused to the damage zone of already existing faults at this site. This is also reflected by increasing fault spacing and therefore decreasing fault core coverage, about constant fault zone coverage and decreasing overlap of fault zones with depth. Of course constant fault zone coverage is also a result of the assumption of depth independent constant fault zone thickness. Thus, it is expected that the fault zone coverage rather should decrease with depth.

The fault properties compiled from the model and literature consist of single values although properties like fault zone thickness can vary by as much as three orders of magnitude within very short distances (Childs *et al.* 2009; Seebeck *et al.* 2014) and most likely is changing from the fault center toward the fault tips (Faulkner *et al.* 2011). The estimation of missing geometric fault zone properties is based on scaling laws derived for strike-slip faults on log-log scale. Most faults at Poehla-Tellerhaeuser Ore Field were reactivated several times within different tectonic regimes and therefore are hybrid faults. Still, most of the faults might have acted as strike-slip faults lately (Table 1).

Formation of mesoscale fractures in fault damage zones

Mesoscale fractures are assumed to dominate the bulk transmissivity of fault damage zones as long as effective stresses remain below about 25 MPa (Mitchell and Faulkner 2012), which corresponds to a depth of about 1.5 km under hydrostatic pressure conditions. A variety of superimposed processes are expected to be responsible for the formation of mesoscale fractures in fault damage zones (Faulkner *et al.* 2011). As the genetic relationships between mesoscale fractures and faults have not been investigated in this project, some of the conductive

mesoscale fractures might also be genetically unrelated to the corresponding fault zones derived from the RCFD and ACFD approach. Our results indicate that the orientation distribution of the conductive mesoscale fractures is not purely stochastic, but that the conductive fractures are rather showing a widened range of orientations as compared to the orientations of the related mining scale fault zones.

Repeated deformation within single faults causes increasing cataclasis which in turn increases transmissivity until a certain threshold is reached (Scholz *et al.* 1993; Faulkner *et al.* 2010). Further shearing reduces transmissivity as the usable pore space volume decreases and retrogressive mineral reactions lead to the formation of clay gouge. Our data indicate that this is not restricted to single faults but that this mechanism might be applicable to fault networks (Table 7). Therefore, the most intensively faulted deposit Haemmerlein is the least transmissive within the Poehla-Tellerhaeuser Ore Field (compare Fig. 4 and 14). Also the comparably low average inflow rates within the entire ore field are attributed to the maturity of the fault system (compare with Masset & Loew 2010; Seebeck *et al.* 2014).

Water flow within mining scale fault zones

Due to the regional scale of the study, multiple fault planes are often merged in the 3D geologic model simplifying the architecture of individual fault zones. As the faults at Poehla-Tellerhaeuser Ore Field were repeatedly reactivated (Hösel 2002; Kuschka 2002; Pälchen & Walter 2011; Schuppan & Hiller 2012), the fault network is presumably in a mature state and the geometry of faults should have the tendency for simple planar geometries (Faulkner *et al.* 2008). This might explain why only two fault zones have been described to be asymmetric (V.I. Velichkin & B.P. Vlasov, unpublished report; Hösel 2002; Schuppan & Hiller 2012). Hence, fault zones in our model are assumed to have a symmetric architecture consisting of fault core, damage zone, and protolith although this is not the case at other sites (Wallace & Morris 1986; Sibson 1996; Faulkner *et al.* 2003, 2011; Wibberley & Shimamoto 2003). Additionally, the thickness of fault zone and fault core is assumed to be independent from the overburden.

Our results demonstrate that most of the inflow or transmissivity is generated within the nearest 30% to 50% of the fault damage zone (Fig. 14). The cumulative inflow decreases exponentially to background levels as the protolith is approached. The normalized graphs reveal similar shapes of an exponential decrease of cumulative flow rates within the deposits but they differ in curvature (Fig. 14B). This decrease in flow rate and cumulative flow rate or transmissivity (Fig. 14B,C) with distance to the fault center might be related to the exponential decrease of mesoscale

fracture spacing in fault damage zones (Faulkner *et al.* 2010) and therefore reveals differences in the governing fault zone architecture and fault zone evolution. The onset of effective inflow in Tellerhaeuser deposit is closer to the fault center and curvature of the normalized cumulative flow rate is steeper in comparison with the Globenstein deposit (Fig. 14A) which might be attributed to a denser fault network with multiple overlapping fault zones (Fig. 4) and therefore shorter distances to the next fault at Tellerhaeuser. Gently dipping faults ($<30^\circ$) are included into the cumulative curve according to their strike. Although they exhibit a significant number of inflows, the influence onto the cumulative curve is marginal (Fig. 8). Effectively no difference would be observed in cumulative flow if those faults were excluded. The equally good results for the two relationship models of inflows and faults (ACFD and RCFD) and for the averaging distance (5%, 10%, and 20%) with about equal exponential factors demonstrate the robustness of the proposed permeability model.

In general, single large inflows stick out and appear randomly distributed in space (Table 4), in orientation (Fig. 8), and in position within the fault zone architecture (Fig. 14A). Similar observation is described in Masset & Loew (2010) for the Gotthard Base Tunnel (Swiss Alps). The assessment of processes leading to very high inflows is difficult because local information on potential key factors such as stress conditions, protolith lithology and elastic properties, fault architecture, fault strength, or fracture mineralization is missing.

Fault zone transmissivity, orientation, and stress state

Water flow in fractured rocks is strongly influenced by the current stress state (e.g., Barton *et al.* 1995; Talbot & Sirat 2001; Cox 2010; Ingebretsen & Appold 2012; Ernest & Boutt 2014). Unfortunately, no stress measurements are available for the Poehla-Tellerhaeuser Ore Field but it can be expected that near surface stresses show larger variations due to topographic effects in comparison with stress conditions substantially below the receiving streams. The orientations of transmissive faults are highly dispersed close to the surface. The depth transition to more focused flow through NE-SW and NW-SE striking faults aligns with the elevation of the valley bottom of the Ohře- (Eger-) Rift which is at about 350–400 masl. Adjacent valley incisions in the ore field are between 150 and 300 m deep. Rock mechanical effects around the outcropping Eibenstock type granites and the Schwarzenberg dome might also contribute to local redistribution of stresses not aligning with the regional stress field close to the surface. NW-SE striking faults are the main transmissive fault zones which might be critically stressed in deeper parts of the ore field considering the regional stress field described in section Site Description.

A sensitivity analysis of transmissivity estimations using the approximation of Jacob & Lohman (1952) was performed by Masset & Loew (2010, 2013). For radial flow to a circular well, the authors estimated stochastically the uncertainty of transmissivity to yield about half an order of magnitude and the mean transmissivity usually being slightly underestimated. In comparison with packer test results, mean $\log T$ estimated from drift or tunnel inflows yield a lower bound of expected values (Mas Ivars 2006; Fernandez & Moon 2010; Masset & Loew 2013). The late time assumption of Jacob's method is violated by 15 individual inflows and their transmissivity is probably underestimated. But as the total number is low (around 1.5% of the entire dataset) and these inflow points are equally distributed within the number of fault zones, they do not have a significant influence on the results. Enhanced transmissivities of NW-SE and NE-SW striking fault zones correlate with the longest activity in different regimes, highest destruction, and therefore the highest extensions of those faults in 3D (Table 1). Finally, these highly transmissive fault zones were most recently active. For these reasons, NW-SE and NE-SW striking fault zones are hydraulically active over larger percentages of the damage zone in comparison with fault zones striking NNW-SSE and N-S as observed within the cumulative flow rate graphs (Fig. 15).

SUMMARY AND CONCLUSIONS

An outstanding dataset has been compiled for the Poehla-Tellerhaeuser Ore Field situated within the western Ore Mountains. It consists mainly of detailed descriptions of groundwater inflows to about 125 km of tunnels and 15 km of drillings documented in archived sampling books, geologic maps, and cross sections of the mining area. All data were compiled and integrated into a 3D geological model. Early time inflow measurements were converted into transmissivities using a simplified analytical solution (Jacob & Lohman 1952), which is valid for constant head drawdown and radial flow to a linear drift or borehole. Mining scale faults with trace length ranging between 0.3 and 30 km have been grouped into five main strike directions, of which NW-SE and NE-SW striking faults are the most frequent both in number of faults and cumulative trace length. Structural fault zone properties (fault core and damage zone thickness, displacement, and length) have been compiled for the investigation area and completed with estimations using generic relationships developed by Kolyukhin & Torabi (2012). The data were used to investigate hydraulic properties of fault zone dominated crystalline basement rocks at site scale, to characterize water flow and transmissivity distribution within fault zones, and investigate their dependence on fault zone architecture, fault orientation, and tectonic history.

The structural properties of the faults at Poehla-Tellerhaeuser Ore Field exhibit rather intensive shearing which is due to a long multiphase tectonic history with several reactivations and/or intensive displacement along the faults. Only NE-SW striking faults indicate relatively smaller displacement and corresponding narrow damage zones. Fault zone coverage was calculated for mining level parallel slices through the 3D geologic model, based on the assumptions that fault zone thickness of the individual fault zone is constant and fault zone architecture is symmetric, consisting of a central fault core, adjacent fault damage zones, and the protolith. On average, fault zone coverage in the investigated volume is very high, around 90%, and in most places several damage zones overlap. The area covered by fault core and the area covered by multiple overlapping fault zones decrease with depth expressing fewer destruction with increasing depth.

Flow rates of 1030 discrete inflows in the range of 1.7E-8 and 3.7E-2 $m^3 \text{ sec}^{-1}$ were quantitatively analyzed, exhibiting close to log-normal flow rate distribution. In comparison, the average values of inflow rates are about one to two orders of magnitude lower than the inflow rates to tunnels determined in similar lithological environment at the southern Taupo Rift in New Zealand (Seebek *et al.* 2014) and in 100-m tunnel intervals in the Swiss Alps (Masset & Loew 2010).

The single inflows from the mesoscale fractures were related to the mining scale faults using two geometrical minimum distance criteria in 3D. 97% of all inflows to the drifts and drillings at Poehla-Tellerhaeuser Ore Field are located within fault zones. Most discrete inflows were situated within one or several intermediate to steeply dipping fault damage zones. The mean fracture transmissivity is highest within up to two overlapping fault zones and decreases with increasing number of fault zone overlaps. This might be related to progressively increased shearing, cataclasis, and retrograde mineral reactions as it has been observed for maturing single faults. Highest single flow rates relate to faults with intermediate dip, which are at least partially related to karstified NE-SW striking marble lenses. The highest fraction of inflows and the highest cumulative flow rates come from NW-SE and NE-SW striking fault zones. Cumulative flow distribution functions within damage zones are exponentially decreasing from the fault center toward the protolith and the curvature seems to depend on fault orientation (and type). 75–95% of the flow occurs in the inner 50% of the damage zone. If flow rate is used as a first order proxy for permeability, none of these graphs follow standard permeability models for fault zones. Although lower flow rates were recognized within most fault centers, a barrier behavior is possibly seen only for fault zones at the Globenstein deposit. The exponential decrease of normalized flow rates and normalized cumulative flow rates toward the protolith agrees with decreasing fracture frequency. Few

exceptionally high inflows seem to be randomly distributed in 3D space and generate a high degree of hydraulic heterogeneity. To our knowledge, this is the first time that a hydraulic model for mining scale faults has been established based on a very large 3D dataset.

Transmissive faults have a very wide orientation distribution in the upper most hundred meters below ground surface (equals about 500–600 masl). In the depth range 150–300 mbgs (about 250–400 masl), two preferred orientations of faults are conductive (NE-SW and NW-SE striking). Below 300 mbgs (about 250 masl), only one strike direction (dipping toward 60° and 240°) is conductive. This depth-dependent orientation of conductive faults might represent variations in the stress field with a topographic overprint due to local valley incisions and the adjacent Ohře- (Eger-) Rift in shallow and intermediate depth, and more stable stress orientations controlled by the regional tectonic regime at depth.

The analyses presented are based on statistical relationships between inflows, fracture transmissivities, and mining scale faults. The relationships between mesoscale fracture transmissivity, depth, lithology, fracture mineralogy, and metamorphic overprint are described and explored in the companion paper.

ACKNOWLEDGEMENTS

We like to thank the Team of the Archive of Wismut GmbH and the Saxon State Agency for Geology, Agriculture and Environment (LfULG) for funding, provision and compilation of data and professional advice, the Public Enterprise for Geobased Information and Surveying of Saxony (GeoSN) for the DEM of Saxony. Further, we thank I. Görz (TU BA Freiberg) and P. Mejias-Herrera (Université de Lorraine) for help concerning the 3D geological modeling and Paradigm for the provision of the SKUA-GOCAD license. Additionally, we thank two anonymous reviewers for valuable improvements and questions.

REFERENCES

- Andreani L, Stanek KP, Gloaguen R, Krentz O, Dominguez-Gonzalez L (2014) DEM-based analysis of interactions between tectonics and landscapes in the Ore Mountains and Eger Rift (East Germany and NW Czech Republic). *Remote Sensing*, **6**, 7971–8001.
- Aydin A (2000) Fractures, faults, and hydrocarbon entrapment, migration and flow. *Marine and Petroleum Geology*, **17**, 797–814.
- Ball LB, Ge S, Caine JS, Revil A, Jardani A (2010) Constraining fault-zone hydrogeology through integrated hydrological and geoelectrical analysis. *Hydrogeology Journal*, **18**, 1057–67.
- Bankwitz P, Gross U, Bankwitz E (1993) Krustendeforrmation im Bereich der Finne-Kyffhäuser-Gera-Jachymov-Zone. *Zeitschrift für Geologische Wissenschaften*, **21**, 3–3.
- Bankwitz P, Bankwitz E, Franzke HJ, Rauche H, Dannapfel M (1995) In situ-Spannungsmessungen in Thüringen und Sachsen. *Brandenburgische Geowissenschaftliche Beiträge*, **2/95**, 77–94.
- Barton CA, Zoback MD, Moos D (1995) Fluid flow along potentially active faults in crystalline rock. *Geology*, **23**, 683–6.
- Bear J, Tsang CF, De Marsily G (1993) *Flow and Contaminant Transport in Fractured Rock*. Academic Press Inc., San Diego.
- Beaudoin G, Therrien R, Savard C (2006) 3D numerical modelling of fluid flow in the Val-d'Or orogenic gold district: major crustal shear zones drain fluids from overpressured vein fields. *Mineralium Deposita*, **41**, 82–98.
- Benedek K, Molnár P (2013) Combining structural and hydrogeological data: conceptualization of a fracture system. *Engineering Geology*, **163**, 1–10.
- Bense VF, Gleeson T, Loveless SE, Bour O, Scibek J (2013) Fault zone hydrogeology. *Earth-Science Reviews*, **127**, 171–92.
- Berger HJ, Felix M, Görne S, Koch E, Krentz O, Förster A, Förster HJ, Konietzky H, Lunow C, Walter K, Schütz H, Stanek K, Wagner S (2011) *Tiefengeothermie Sachsen-1. Arbeitsetappe 09/2009–07/2010*. Landesamt für Umwelt, Landwirtschaft und Geologie, Freistaat Sachsen, Freiberg-Dresden.
- Berkowitz B (2002) Characterizing flow and transport in fractured geological media: a review. *Advances in Water Resources*, **25**, 861–84.
- Buchholz P, Korn M, Wendt S, Funke S, Hänel F, Mittag R, Burghardt T, Rappisilber I, Wallner O, Krentz O, Witthauer B, Novak E (2011) *Erdbebenbeobachtung im Freistaat Sachsen - Dreijahresbericht 2007–2009*. <http://nbn-resolving.de/urn:nbn:de:bsz:14-qucosa-70241>, Sächsisches Landesamt für Umwelt, Landwirtschaft und Geologie.
- Byerlee J (1993) Model for episodic flow of high-pressure water in fault zones before earthquakes. *Geology*, **21**, 303–6.
- Caine JS, Forster CB (1999) Fault zone architecture and fluid flow: insights from field data and numerical modeling. In: *Faults and Subsurface Fluid Flow in the Shallow Crust*. Vol. **113**, pp. 101–27. American Geophysical Union Geophysical Monograph, Washington, D. C.
- Caine JS, Evans JP, Forster CB (1996) Fault zone architecture and permeability structure. *Geology*, **24**, 1025–8.
- Caine JS, Bruhn RL, Forster CB (2010) Internal structure, fault rocks, and inferences regarding deformation, fluid flow, and mineralization in the seismogenic Stillwater normal fault, Dixie Valley, Nevada. *Journal of Structural Geology*, **32**, 1576–89.
- Chester FM, Logan JM (1987) Composite planar fabric of gouge from the Punchbowl Fault, California. *Journal of Structural Geology*, **9**, 621–6.
- Childs C, Manzocchi T, Walsh JJ, Bonson CG, Nicol A, Schöpfer MPJ (2009) A geometric model of fault zone and fault rock thickness variations. *Journal of Structural Geology*, **31**, 117–27.
- Cox SF (2010) The application of failure mode diagrams for exploring the roles of fluid pressure and stress states in controlling styles of fracture-controlled permeability enhancement in faults and shear zones. *Geofluids*, **10**, 217–33.
- Earnest E, Boutt D (2014) Investigating the role of hydromechanical coupling on flow and transport in shallow fractured-rock aquifers. *Hydrogeology Journal*, **22**, 1573–91.
- Evans JP, Forster CB, Goddard JV (1997) Permeability of fault-related rocks, and implications for hydraulic structure of fault zones. *Journal of Structural Geology*, **19**, 1393–404.
- Faulkner DR, Lewis AC, Rutter EH (2003) On the internal structure and mechanics of large strike-slip fault zones: field

- observations of the Carboneras fault in southeastern Spain. *Tectonophysics*, **367**, 235–51.
- Faulkner DR, Mitchell TM, Healy D, Heap MJ (2006) Slip on ‘weak’ faults by the rotation of regional stress in the fracture damage zone. *Nature*, **444**, 922–5.
- Faulkner DR, Mitchell TM, Rutter EH, Cembrano J (2008) On the structure and mechanical properties of large strike-slip faults. *Geological Society, London, Special Publications*, **299**, 139–50.
- Faulkner DR, Jackson CAL, Lunn RJ, Schlische RW, Shipton ZK, Wibberley CAJ, Withjack MO (2010) A review of recent developments concerning the structure, mechanics and fluid flow properties of fault zones. *Journal of Structural Geology*, **32**, 1557–75.
- Faulkner DR, Mitchell TM, Jensen E, Cembrano J (2011) Scaling of fault damage zones with displacement and the implications for fault growth processes. *Journal of Geophysical Research: Solid Earth*, **116**, 11.
- Fernandez G, Moon J (2010) Excavation-induced hydraulic conductivity reduction around a tunnel – Part 1: guideline for estimate of ground water inflow rate. *Tunnelling and Underground Space Technology*, **25**, 560–6.
- Forster CB, Evans JP (1991) Hydrogeology of thrust faults and crystalline thrust sheets: results of combined field and modeling studies. *Geophysical Research Letters*, **18**, 979–82.
- Gale JE (1982) Assessing the permeability characteristics of fractured rock. *Geological Society of America Special Papers*, **189**, 163–82.
- Gentier S, Hopkins D, Riss J (2013) Role of fracture geometry in the evolution of flow paths under stress. In: *Dynamics of Fluids in Fractured Rock* (eds Faybishenko B, Witherspoon PA, Benson SM), Vol. **122**, pp. 169–184. American Geophysical Union, Washington, D. C.
- Grünthal G, Stromeyer D (1992) The recent crustal stress field in central Europe: trajectories and finite element modeling. *Journal of Geophysical Research: Solid Earth*, **97**, 11805–20.
- Grünthal G, Schenk V, Zeman A, Schenková Z (1990) Seismotectonic model for the earthquake swarm of 1985–1986 in the Vogtland/West Bohemia focal area. *Tectonophysics*, **174**, 369–83.
- Guyonnet D, Lavanchy JM (1992) Analysis of single-and cross-hole tests at the BK-site, Grimsel Test Site. In: *Interpretation of Crosshole Hydraulic Tests and a Pilot Fluid Logging Test for Selected Boreholes within the BK Site*. Nagra Technical Report 91–09 (eds Vomvoris S, Frieg B), pp. 31–71. Nagra, Wettingen.
- Heidbach O, Tingay M, Barth A, Reinecker J, Kurfeß D, Müller B (2008) The world stress map database release 2008. *Tectonophysics*, **482**, 3–15.
- Henriksen H (1995) Relation between topography and well yield in boreholes in crystalline rocks, Sogn og Fjordane, Norway. *Ground Water*, **33**, 635–43.
- Hiller A (1995) Geologischer Bau der Lagerstaetten Haemmerlein und Tellerhaeuser im Westerzgebirge. *Zeitschrift für Geologische Wissenschaften*, **23**, 599–608.
- Hiller A, Härtel T, Reinhold E (2013) *Recherche und Zusammenstellung montanhydrogeologischer Sachverhalte ausgewählter Bergbaureviere - Teil I*. Wismut GmbH, Hartenstein.
- Horálek J, Fischer T, Boušková A, Jedlička P (2000) The Western Bohemia/Vogtland region in the light of the WEBNET network. *Studia Geophysica et Geodaetica*, **44**, 107–25.
- Hösel G (2002) *Die polymetallische Skarnlagerstätte Pöhlberg-Globenstein*. Sächsisches Landesamt für Umwelt und Geologie (LfUG).
- Ingebritsen SE, Appold MS (2012) The physical hydrogeology of ore deposits. *Economic Geology*, **107**, 559–84.
- Ingebritsen SE, Gleeson T (2015) Crustal permeability: introduction to the special issue. *Geofluids*, **15**, 1–10.
- Ingebritsen SE, Manning CE (2010) Permeability of the continental crust: dynamic variations inferred from seismicity and metamorphism. *Geofluids*, **10**, 193–205.
- Jacob CE, Lohman SW (1952) Nonsteady flow to a well of constant drawdown in an extensive aquifer. *Eos, Transactions of the American Geophysical Union*, **33**, 559–69.
- Kolyukhin D, Torabi A (2012) Statistical analysis of the relationships between faults attributes. *Journal of Geophysical Research: Solid Earth*, **117**, B05406. doi:10.1029/2011JB008880.
- Kuschka E (ed.) (2002) *Zur Tektonik, Verbreitung und Minerogenie sächsischer hydrothermaler Mineralgänge*. Sächsisches Landesamt für Umwelt und Geologie, Freiberg/Flöha.
- Lachassagne P, Wyns R, Dewandel B (2011) The fracture permeability of hard rock aquifers is due neither to tectonics, nor to unloading, but to weathering processes. *Terra Nova*, **23**, 145–61.
- Lawson DW (1968) Groundwater flow systems in the crystalline rocks of the Okanagan Highland, British Columbia. *Canadian Journal of Earth Sciences*, **5**, 813–24.
- Lilliefors HW (1967) On the Kolmogorov-Smirnov test for normality with mean and variance unknown. *Journal of the American Statistical Association*, **62**, 399–402.
- Long JCS, Aydin A, Brown SR, Einstein HH, Hestir K, Hsieh PA, Myer LR, Nolte KG, Norton DL, Olsson OL, Paillet FL, Smith JL, Thomson L (1996) *Rock Fractures and Fluid Flow: Contemporary Understanding and Applications*. National Academies Press, Washington, D. C.
- Lützenkirchen VH (2002) *Structural geology and hydrogeology of brittle fault zones in the central and eastern Gotthard massif, Switzerland*. Diss., Naturwissenschaften, Eidgenössische Technische Hochschule ETH Zürich, Nr. 14749, 2003.
- Maréchal JC (1998) *Les circulations d'eau dans les massifs cristallins alpins et leurs relations avec les ouvrages souterrains*. École Polytechnique Fédérale de Lausanne.
- Maréchal JC, Dewandel B, Subrahmanyam K (2004) Use of hydraulic tests at different scales to characterize fracture network properties in the weathered-fractured layer of a hard rock aquifer. *Water Resources Research*, **40**, W11508.
- Mas Ivars D (2006) Water inflow into excavations in fractured rock—a three-dimensional hydro-mechanical numerical study. *International Journal of Rock Mechanics and Mining Sciences*, **43**, 705–25.
- Masset O, Loew S (2010) Hydraulic conductivity distribution in crystalline rocks, derived from inflows to tunnels and galleries in the Central Alps, Switzerland. *Hydrogeology Journal*, **18**, 863–91.
- Masset O, Loew S (2013) Quantitative hydraulic analysis of pre-drillings and inflows to the Gotthard Base Tunnel (Sedrun Lot, Switzerland). *Engineering Geology*, **164**, 50–66.
- Massey FJ Jr (1951) The Kolmogorov-Smirnov test for goodness of fit. *Journal of the American Statistical Association*, **46**, 68–78.
- Massonnat G (1981) *Hydrogéologie en milieu fissuré et thermalisme-Etude du massif de Bramefarine et du nord du massif d'Allevard-La source thermominérale d'Allevard (Isère-France)-Alpes françaises*. Université Scientifique et Médicale de Grenoble.
- Micklethwaite S, Sheldon HA, Baker T (2010) Active fault and shear processes and their implications for mineral deposit formation and discovery. *Journal of Structural Geology*, **32**, 151–65.
- Miller SA, Nur A (2000) Permeability as a toggle switch in fluid-controlled crustal processes. *Earth and Planetary Science Letters*, **183**, 133–46.

- Mitchell TM, Faulkner DR (2012) Towards quantifying the matrix permeability of fault damage zones in low porosity rocks. *Earth and Planetary Science Letters*, **339**, 24–31.
- Mori A, Mazurek M, Adler M, Schild M, Siegesmund S, Vollbrecht A, Ota K, Ando T, Alexander WR, Smith P (2003) *The Nagra-JNC in situ study of safety relevant radionuclide retardation in fractured crystalline rock IV: The in situ study of matrix porosity in the vicinity of a water conducting fracture May 2003*. TECHNISCHER BERICHT-NAGRA NTB.
- Neuman SP (2005) Trends, prospects and challenges in quantifying flow and transport through fractured rocks. *Hydrogeology Journal*, **13**, 124–47.
- Pälchen W, Walter H (2011) *Geologie von Sachsen I: Geologischer Bau und Entwicklungsgeschichte*. E. Schweizerbart'sche Verlagsbuchhandlung (Nägele u. Obermiller), Stuttgart.
- Pan E, Amadei B, Savage WZ (1994) Gravitational stresses in long symmetrical ridges and valleys in anisotropic rock. *International Journal of Rock Mechanics and Mining Sciences & Geomechanics Abstracts*, **31**, 293–312.
- Pan E, Amadei B, Savage WZ (1995) Gravitational and tectonic stresses in anisotropic rock with irregular topography. *International Journal of Rock Mechanics and Mining Sciences & Geomechanics Abstracts*, **32**, 201–14.
- Roques C, Bour O, Aquilina L, Dewandel B, Leray S, Schroetter JM, Longuevergne L, Le Borgne T, Hochreutener R, Labasque T, Lavenant N, Vergnaud-Ayraud V, Mougin B (2014) Hydrological behavior of a deep sub-vertical fault in crystalline basement and relationships with surrounding reservoirs. *Journal of Hydrology*, **509**, 42–54.
- Rutqvist J, Stephansson O (2003) The role of hydromechanical coupling in fractured rock engineering. *Hydrogeology Journal*, **11**, 7–40.
- Scholz CH, Dawers NH, Yu JZ, Anders MH, Cowie PA (1993) Fault growth and fault scaling laws: preliminary results. *Journal of Geophysical Research: Solid Earth*, **98**, 21951–61.
- Schuppan W, Hiller A (2012) *Die Komplexlagerstätten Tellerhäuser und Hämerlein - Uranbergbau und Zinnerkundung in der Grube Pöhla der SDAG Wismut*. Sächsisches Landesamt für Umwelt, Landwirtschaft und Geologie (LfULG), Freiberg.
- Sebastian U (2012) *Die Geologie des Erzgebirges*. Springer Verlag, Berlin & Heidelberg.
- Seebeck H, Nicol A, Walsh JJ, Childs C, Beetham RD, Pettinga J (2014) Fluid flow in fault zones from an active rift. *Journal of Structural Geology*, **62**, 52–64.
- Seront B, Wong T-F, Caine JS, Forster CB, Bruhn RL, Fredrich JT (1998) Laboratory characterization of hydromechanical properties of a seismogenic normal fault system. *Journal of Structural Geology*, **20**, 865–81.
- Sibson RH (1982) Fault zone models, heat flow, and the depth distribution of earthquakes in the continental crust of the United States. *Bulletin of the Seismological Society of America*, **72**, 151–63.
- Sibson RH (1996) Structural permeability of fluid-driven fault-fracture meshes. *Journal of Structural Geology*, **18**, 1031–42.
- Snow DT (1965) *A Parallel Plate Model of Fractured Permeable Media*. University of California, Berkeley.
- Stober I, Bucher K (2015) Hydraulic conductivity of fractured upper crust: insights from hydraulic tests in boreholes and fluid-rock interaction in crystalline basement rocks. *Geofluids*, **15**, 161–78.
- Sutherland R, Toy VG, Townend J, Cox SC, Eccles JD, Faulkner DR, Prior DJ, Norris RJ, Mariani E, Boulton C, Carpenter BM, Menzies CD, Little TA, Hasting M, De Pascale GP, Langridge RM, Scott HR, Lindroos ZR, Fleming B, Kopf AJ (2012) Drilling reveals fluid control on architecture and rupture of the Alpine fault, New Zealand. *Geology*, **40**, 1143–6.
- Talbot CJ, Sirat M (2001) Stress control of hydraulic conductivity in fracture-saturated Swedish bedrock. *Engineering Geology*, **61**, 145–53.
- Torabi A, Berg SS (2011) Scaling of fault attributes: a review. *Marine and Petroleum Geology*, **28**, 1444–60.
- Tsang C-F, Niemi A (2013) Deep hydrogeology: a discussion of issues and research needs. *Hydrogeology Journal*, **21**, 1687–90.
- Wallace RE, Morris HT (1986) Characteristics of faults and shear zones in deep mines. *Pure and Applied Geophysics*, **124**, 107–25.
- Welch LA, Allen DM (2014) Hydraulic conductivity characteristics in mountains and implications for conceptualizing bedrock groundwater flow. *Hydrogeology Journal*, **00**, 1–24.
- Wibberley CAJ, Shimamoto T (2003) Internal structure and permeability of major strike-slip fault zones: the Median Tectonic Line in Mie Prefecture, Southwest Japan. *Journal of Structural Geology*, **25**, 59–78.

SUPPORTING INFORMATION

Additional Supporting Information may be found online in the supporting information tab for this article:

Figure S1. Flow chart of geologic modelling.

Table S1. Drift directions within the Poehla-Tellerhaeuser Ore Field grouped according to the main strike directions of the faults.

Table S2. Data sources for the geologic 3D model, the hydrogeological and structural geologic datasets.

Table S3. Database of the compiled inflows analyzed in this article.